

# Sensitivity of neutron radii in a $^{208}\text{Pb}$ nucleus and a neutron star to nucleon-sigma-rho coupling corrections in relativistic mean field theory

G. Shen,<sup>1</sup> J. Li,<sup>1</sup> G. C. Hillhouse,<sup>1, 2,\*</sup> and J. Meng<sup>1, 3, 4, †</sup>

<sup>1</sup>*School of Physics, Peking University, Beijing 100871*

<sup>2</sup>*Department of Physics, University of Stellenbosch, Stellenbosch, South Africa*

<sup>3</sup>*Institute of Theoretical Physics, Chinese Academy of Science, Beijing 100080*

<sup>4</sup>*Center of Theoretical Nuclear Physics, National Laboratory of  
Heavy Ion Accelerator, Lanzhou 730000*

(Dated: February 9, 2008)

## Abstract

We study the sensitivity of the neutron skin thickness,  $S$ , in a  $^{208}\text{Pb}$  nucleus to the addition of nucleon-sigma-rho coupling corrections to a selection (PK1, NL3, S271, Z271) of interactions in relativistic mean field model. The PK1 and NL3 effective interactions lead to a minimum value of  $S = 0.16$  fm in comparison with the original value of  $S = 0.28$  fm. The S271 and Z271 effective interactions yield even smaller values of  $S = 0.11$  fm, which are similar to those for nonrelativistic mean field models. A precise measurement of the neutron radius, and therefore  $S$ , in  $^{208}\text{Pb}$  will place an important constraint on both relativistic and nonrelativistic mean field models. We also study the correlation between the radius of a 1.4 solar-mass neutron star and  $S$ .

PACS numbers: 21.10.-k, 21.10.Gv, 26.60.+c, 27.80.+w

---

\*e-mail: gch@sun.ac.za

†e-mail: mengj@pku.edu.cn

## I. INTRODUCTION

Precise values for proton and neutron densities in nuclei, as well as their corresponding root-mean-square (rms) radii, are very important for providing quantitative predictions in nuclear physics and nuclear astrophysics. Our present understanding of nuclear phenomena largely hinges on accurate and model independent determinations of charge densities and radii via electron scattering. However, this picture of the nucleus will be more complete once precise values for neutron radii become available. Currently, the situation regarding the experimental determination of neutron radii is unsatisfactory with errors typically being an order of magnitude larger than those for proton radii [1]. What is more disconcerting, however, is the large variation in quoted values of the neutron radius for a single nucleus such as  $^{208}\text{Pb}$  [2, 3, 4, 5, 6, 7]. This dismal situation has prompted an experiment at Jefferson Laboratory [8] to measure the neutron radius in  $^{208}\text{Pb}$  accurately and model independently via parity-violating electron scattering, the results of which are expected to have a widespread and important impact in nuclear physics.

Reliable neutron densities and radii are needed for quantitatively characterizing the bulk properties of nuclear matter at normal nuclear densities, which in turn serve as valuable input for: studying the dynamics of heavy-ion collisions, determining the equation-of-state which underpins the evolution and structure of supernovae and neutron stars, studying the properties of exotic neutron-rich nuclei far from the beta-stability line, reducing uncertainties in atomic parity violation experiments, as well as for studying pionic and antiprotonic atoms.

Recently, much attention [2, 3, 4, 5, 6, 7, 9, 10, 11] has been devoted to studying the neutron skin thickness,  $S$ , in  $^{208}\text{Pb}$ , a quantity which is defined as the difference between the rms radius of neutrons,  $\sqrt{\langle r_n^2 \rangle}$ , and protons,  $\sqrt{\langle r_p^2 \rangle}$ , *i.e.*,  $S = \sqrt{\langle r_n^2 \rangle} - \sqrt{\langle r_p^2 \rangle}$ . A precise measurement of the neutron radius of  $^{208}\text{Pb}$ , together with existing high-precision measurements of the proton radius [12], will yield a precise value for the neutron skin thickness, thus providing one of the most stringent tests to date for current models of nuclear structure. Indeed, the Parity Radius Experiment at Jefferson Laboratory aims to measure the neutron radius in  $^{208}\text{Pb}$  to an unprecedented accuracy of 1% ( $\pm 0.05$  fm). Currently relativistic and nonrelativistic models predict completely different values for the neutron radius and, hence, it is evident that the latter measurement will have an impact on deepening our understanding of the dynamical basis of nuclear structure. In particular, nonrelativistic

Skyrme models predict  $S = 0.1 \sim 0.2$  fm [9, 10, 11], whereas present relativistic mean field (RMF) models, on the other hand, give  $S = 0.2 \sim 0.3$  fm [9, 11]. Model-dependent analyses of experimental data with hadronic probes yield values of  $S$  varying between 0.0 and 0.2 fm (see Table I), which seem to be more consistent with the predictions of nonrelativistic models based on the Schrödinger equation. Hadronic measurements, however, suffer from potentially serious theoretical systematic errors associated with uncertainties in nuclear reaction mechanisms and, hence, one should be cautious about drawing conclusions regarding the appropriateness of various dynamical models.

In this paper we focus on a relativistic description of nuclei and neutron stars within the field theoretical framework of quantum hydrodynamics. In particular, we capitalize on the success of the Walecka model and extensions thereof to successfully describe the properties of nuclear matter and finite nuclei [13, 14, 15, 16, 17], as well as predict the well-known central and spin-orbit potentials which are usually postulated in nonrelativistic Schrödinger-equation-based models [18, 19, 20, 21]. More specifically, we supplement existing relativistic mean field Lagrangian densities with two new isospin dependent higher order correction terms relating to the coupling of the nucleon current to sigma- and rho-meson fields. These terms can be associated with multi-meson exchange processes occurring in the inner higher-density region of nuclei. In low-energy nucleon-nucleon scattering models, the contribution to the scattering amplitudes is usually dominated by single-meson exchange with an effective mass of less than 1 GeV. However, it has been demonstrated that the inclusion of two-meson exchange at low energies provides a major improvement in the description of nucleon-nucleon scattering data [22]. In general there is no unique way for introducing nonlinear isovector-nucleon couplings in relativistic mean field models. In this paper we introduce the simplest structure generating the nonlinear isospin-dependent terms. Values for the various combinations of the new coupling constants are extracted by fitting to the properties of nuclear matter – such as saturation density, binding energy per nucleon, nuclear incompressibility and the symmetry energy – and the corresponding values for the neutron skin thickness in  $^{208}\text{Pb}$  are extracted for a selection of RMF models. In particular, we focus on the PK1 [23], NL3 [24], S271 and Z271 [25] RMF parameterizations.

One of the issues we wish to address in the paper is to find ways of adjusting the neutron radius in  $^{208}\text{Pb}$  by adding new terms to the Lagrangian density of existing relativistic mean field models, while at the same time keeping the value of proton radius (which is accurately

determined experimentally) fixed. In particular, the question arises as to whether it is possible for RMF models to produce values of the neutron radius which are in the same range as those for nonrelativistic models.

In recent analyses, a linear relationship between the neutron skin in  $^{208}\text{Pb}$  and the nuclear symmetry energy at saturation density was proposed [10, 11, 26]. We also investigate the relationship between the latter quantities for our new RMF models. The new interaction terms considered in this paper influence the density dependence of symmetry energy, which in turn affects the neutron skin in  $^{208}\text{Pb}$ . In addition, we extrapolate from normal to dense neutron matter and study the correlation between the radius of a neutron star and the neutron radius in  $^{208}\text{Pb}$ . Indeed, Horowitz and Piekarewicz [27] have performed such a correlation analysis for a wide range of RMF models and they concluded that, whereas the radius of a 0.5 solar-mass neutron star can be inferred from the radius of  $^{208}\text{Pb}$ , the radius of a 1.4 solar-mass neutron star is not uniquely constrained by a measurement of the neutron skin thickness. In this paper we perform a similar analysis for the PK1, NL3, S271 and Z271 effective interactions supplemented with our new terms, but for simplicity we only consider the mass and radius of a 1.4 solar-mass neutron star.

This paper is organized in the following sequence. A brief formulation of our new RMF model in relation to existing RMF models for finite nuclei and neutron star matter is presented in Sec. II. The extraction of parameter sets for our new RMF models is discussed in Sec. III. In Sec. IV results are presented and discussed for the neutron radius in  $^{208}\text{Pb}$ . Values of neutron radii in  $^{208}\text{Pb}$  for different parameter sets are then correlated with the radius of a 1.4 solar-mass neutron star. Finally, in Sec. V, we summarize the main points of this paper.

## II. HIGHER ORDER CORRECTIONS TO RMF MODELS FOR SPHERICAL NUCLEI AND NEUTRON STARS

The basic physics underlying RMF models and their application in nuclear physics can be found in Refs. [28, 29, 30]. In this section we present our new RMF model and indicate its relation to existing RMF models. The basic ansatz of the RMF theory is a Lagrangian density whereby nucleons are described as Dirac particles which interact via the exchange

of sigma- ( $\sigma$ ), omega- ( $\omega$ ), and rho- ( $\rho$ ) mesons, and also the photons ( $A$ ), namely:

$$\begin{aligned}\mathcal{L} = & \bar{\psi} \left[ i\gamma^\mu \partial_\mu - m - g_\sigma \sigma - g_\omega \gamma^\mu \omega_\mu - g_\rho \gamma^\mu \vec{\tau} \cdot \vec{\rho}_\mu - e\gamma^\mu \frac{1+\tau_3}{2} A_\mu \right] \psi \\ & + \frac{1}{2} \partial^\mu \sigma \partial_\mu \sigma - \frac{1}{2} m_\sigma^2 \sigma^2 - U(\sigma) \\ & - \frac{1}{4} \omega^{\mu\nu} \omega_{\mu\nu} + \frac{1}{2} m_\omega^2 \omega^\mu \omega_\mu + U(\omega) \\ & - \frac{1}{4} \vec{\rho}^{\mu\nu} \cdot \vec{\rho}_{\mu\nu} + \frac{1}{2} m_\rho^2 \vec{\rho}^\mu \cdot \vec{\rho}_\mu \\ & - \frac{1}{4} A^{\mu\nu} A_{\mu\nu}\end{aligned}\tag{1}$$

where the field tensors of the vector mesons and the electromagnetic field take the following form:

$$\begin{aligned}\omega^{\mu\nu} &= \partial^\mu \omega^\nu - \partial^\nu \omega^\mu, \\ A^{\mu\nu} &= \partial^\mu A_\nu - \partial^\nu A_\mu, \\ \vec{\rho}^{\mu\nu} &= \partial^\mu \vec{\rho}^\nu - \partial^\nu \vec{\rho}^\mu - g_\rho \vec{\rho}^\mu \times \vec{\rho}^\nu.\end{aligned}\tag{2}$$

The nonlinear self-couplings for  $\sigma$  and  $\omega$  mesons are respectively:

$$U(\sigma) = \frac{1}{3} g_2 \sigma^3 + \frac{1}{4} g_3 \sigma^4, \quad U(\omega) = \frac{1}{4} c_3 (\omega^\mu \omega_\mu)^2,\tag{3}$$

with the self-coupling constants  $g_2$ ,  $g_3$ , and  $c_3$ .

To modify the density dependence of nuclear matter symmetry energy, Horowitz and Piekarewicz [25] introduced the following nonlinear omega-rho coupling term:

$$\mathcal{L}_{HP} = 4\Lambda_v g_\rho^2 \vec{\rho}_\mu \cdot \vec{\rho}^\mu g_\omega^2 \omega_\mu \omega^\mu.\tag{4}$$

In addition to considering the above term, in this paper we introduce, for the first time, the following two new couplings of the nucleon current to sigma- and rho-meson fields:

$$\mathcal{L}_1 = -\Gamma_1 \bar{\psi} g_\rho \gamma^\mu (g_\sigma \sigma / m) \vec{\tau} \cdot \vec{\rho}_\mu \psi\tag{5}$$

$$\mathcal{L}_2 = -\Gamma_2 \bar{\psi} g_\rho \gamma^\mu (g_\sigma \sigma / m)^2 \vec{\tau} \cdot \vec{\rho}_\mu \psi\tag{6}$$

*i.e.*, the total Lagrangian density of interest is:

$$\mathcal{L}' = \mathcal{L} + \mathcal{L}_{HP} + \mathcal{L}_1 + \mathcal{L}_2.\tag{7}$$

The classical variational principle leads to the following equations of motion:

$$[\alpha \cdot \mathbf{p} + V(\mathbf{r}) + \beta(m + S(\mathbf{r}))]\psi_i = \varepsilon_i \psi_i \quad (8)$$

for the nucleon spinors, where

$$\begin{cases} V(\mathbf{r}) = \beta\{g_\omega\psi_\mu + g_\rho(1 + \Gamma_1(g_\sigma\sigma/m) + \Gamma_2(g_\sigma\sigma/m)^2)\vec{\rho}_\mu \cdot \vec{\rho}_\mu + e\frac{(1+\tau_3)}{2}A_\mu\} \\ S(\mathbf{r}) = g_\sigma\sigma \end{cases} \quad (9)$$

and

$$\begin{cases} (m_\sigma^2 - \nabla^2)\sigma = -g_\sigma\rho_s - g_2\sigma^2 - g_3\sigma^3 - g_\rho\vec{\rho}_\mu \cdot \vec{j}^\mu(\Gamma_1(g_\sigma\sigma/m) + 2\Gamma_2(g_\sigma^2\sigma/m^2)) \\ (m_v^2 - \nabla^2)\omega^\mu = g_\omega j^\mu - c_3\omega^\mu(\omega^\mu\omega_\mu) - 8\Lambda_v g_\rho^2 g_\omega^2 \vec{\rho}_\mu \cdot \vec{\rho}^\mu \omega^\mu \\ (m_\rho^2 - \nabla^2)\vec{\rho}^\mu = g_\rho j^\mu(1 + \Gamma_1(g_\sigma\sigma/m) + \Gamma_2(g_\sigma\sigma/m)^2) - 8\Lambda_v g_\rho^2 g_\omega^2 \omega_\mu \omega^\mu \vec{\rho}^\mu \\ -\nabla^2 A^\mu = ej_p^\mu \end{cases} \quad (10)$$

for the mesons and photons. The nucleon spinors provide the relevant source terms:

$$\begin{cases} \rho_s = \sum_{i=1}^A \bar{\psi}_i \psi_i \\ j^\mu = \sum_{i=1}^A \bar{\psi}_i \gamma^\mu \psi_i \\ \vec{j}^\mu = \sum_{i=1}^A \bar{\psi}_i \gamma^\mu \vec{\tau} \psi_i \\ j_p^\mu = \sum_{i=1}^A \bar{\psi}_i \gamma^\mu \frac{1+\tau_3}{2} \psi_i \end{cases}$$

where the summations run over the valence nucleons only. The present method neglects the contribution of negative energy states, *i.e.* the so-called no sea approximation. The above non-linear equations are solved by iteration within the context of the mean field approximation whereby the meson field operators are replaced by their expectation values.

### A. Spherical nuclei

Since spherical nuclei such as  $^{208}\text{Pb}$  respect time reversal symmetry, there are no currents in the nucleus and the spatial vector components  $\boldsymbol{\omega}$ ,  $\boldsymbol{\rho}$  and  $\boldsymbol{A}$  vanish. One is left with the time-like components  $\omega_0$ ,  $\rho_0$  and  $A_0$ . Charge conservation guarantees that only the 3-components of the isovector  $\rho_{0,3}$  survive. As the system obeys rotational symmetry, the nucleon potentials and the meson-field sources depend only on the radial coordinate  $r$ . The Dirac spinor,  $\psi(r)$  is characterized by the angular momentum quantum numbers  $l, j, m$ ,

the isospin  $t = +(-)$  for protons (neutrons) respectively, and any other relevant quantum numbers  $i$ , i.e.

$$\psi(r) = \begin{pmatrix} i\frac{G_i^{lj}(r)}{r} Y_{jm}^l(\theta, \phi) \\ \frac{F_i^{lj}(r)}{r} (\vec{\sigma} \cdot \hat{r}) Y_{jm}^l(\theta, \phi) \end{pmatrix} \chi_t \quad (11)$$

where  $Y_{jm}^l(\theta, \phi)$  are the usual spinor spherical harmonics,  $G_i^{lj}(r)/r$  and  $F_i^{lj}(r)/r$  denote the upper- and lower-component radial wave functions, and  $\chi_t$  represents the isospin wave functions specified by the isospin  $t$ . The radial wave functions are normalized as:

$$\int_0^\infty dr (|G_i^{lj}(r)|^2 + |F_i^{lj}(r)|^2) = 1. \quad (12)$$

The following phase convention is adopted for the vector spherical harmonics:

$$(\vec{\sigma} \cdot \hat{r}) Y_{jm}^l = -Y_{jm}^{l'},$$

where

$$l' = 2j - l = \begin{cases} l+1, & j = l+1/2, \\ l-1, & j = l-1/2. \end{cases}$$

After some tedious algebra, one gets the radial equation for the upper and lower components, respectively [13]:

$$\begin{cases} \epsilon_i G_i^{lj}(r) = \left( -\frac{\partial}{\partial r} + \frac{\kappa_i}{r} \right) F_i^{lj}(r) + (m + S(r) + V(r)) G_i^{lj}(r) \\ \epsilon_i F_i^{lj}(r) = \left( +\frac{\partial}{\partial r} + \frac{\kappa_i}{r} \right) G_i^{lj}(r) - (m + S(r) - V(r)) F_i^{lj}(r) \end{cases} \quad (13)$$

where

$$\kappa = \begin{cases} -(j+1/2), & \text{for } j = l+1/2, \\ +(j+1/2), & \text{for } j = l-1/2, \end{cases}$$

and

$$\begin{cases} V(r) = g_\omega \omega_0 + g_\rho (1 + \Gamma_1(g_\sigma \sigma/m) + \Gamma_2(g_\sigma \sigma/m)^2) \tau_3 \rho_{0,3} + \frac{1}{2} e(1 + \tau_3) A_0, \\ S(r) = g_\sigma \sigma. \end{cases} \quad (14)$$

The meson fields equations reduce to radial Laplace equations of the form:

$$\left( \frac{\partial^2}{\partial r^2} - \frac{2}{r} \frac{\partial}{\partial r} + m_\phi^2 \right) \phi = S_\phi \quad (15)$$

where  $m_\phi$  are the meson masses for  $\phi = \sigma, \omega, \rho$  and  $m_\phi = 0$  for the photon. The relevant source terms are:

$$S_\phi = \begin{cases} -g_\sigma\rho_s - g_2\sigma^2 - g_3\sigma^3 - g_\rho\rho_{0,3}\rho_3(\Gamma_1(g_\sigma\sigma/m) + 2\Gamma_2(g_\sigma^2\sigma/m^2)) & \text{for the } \sigma \text{ field,} \\ g_\omega\rho_v - c_3\omega_0^3 - 8\Lambda_v g_\rho^2 g_\omega^2 \rho_{0,3}^2 \omega_0 & \text{for the } \omega \text{ field,} \\ g_\rho\rho_3(1 + \Gamma_1(g_\sigma\sigma/m) + \Gamma_2(g_\sigma\sigma/m)^2) - 8\Lambda_v g_\rho^2 g_\omega^2 \omega_0^2 \rho_{0,3} & \text{for the } \rho \text{ field,} \\ e\rho_c(r) & \text{for the Coulomb field,} \end{cases} \quad (16)$$

where the various nucleon densities are given by:

$$\begin{cases} 4\pi r^2 \rho_s(r) = \sum_{i=1}^A (|G_i(r)|^2 - |F_i(r)|^2), \\ 4\pi r^2 \rho_v(r) = \sum_{i=1}^A (|G_i(r)|^2 + |F_i(r)|^2), \\ 4\pi r^2 \rho_3(r) = \sum_{i=1}^Z (|G_i(r)|^2 + |F_i(r)|^2) - \sum_{i=1}^N (|G_i(r)|^2 + |F_i(r)|^2), \\ 4\pi r^2 \rho_c(r) = \sum_{i=1}^Z (|G_i(r)|^2 + |F_i(r)|^2). \end{cases} \quad (17)$$

The neutron and proton rms radii are directly related to the neutron and proton density distributions via the following relationship:

$$R_i = \sqrt{\langle r_i^2 \rangle} = \sqrt{\frac{\int \rho_i(r) r^2 d^3r}{\int \rho_i(r) d^3r}} \quad (18)$$

where  $\rho_i(r)$  ( $i = n, p$ ) denotes the corresponding neutron and proton baryon density distributions.

The total binding energy of the system is:

$$\begin{aligned} E &= E_{nucleon} + E_\sigma + E_\rho + E_\omega + E_c - mA \\ &= \sum_i \epsilon_i - \frac{1}{2} \int d^3r \{ g_\sigma \sigma \rho_s(r) + \frac{1}{3} g_2 \sigma^3 + \frac{1}{2} g_3 \sigma^4 \} \\ &\quad - \frac{1}{2} \int d^3r g_\rho \rho_{0,3} \{ (1 + 2\Gamma_1 \frac{g_\sigma \sigma}{m} + 3\Gamma_2 (\frac{g_\sigma \sigma}{m})^2) \rho_3(r) - 8\Lambda_v (g_\omega \omega_0 g_\rho \rho_{0,3})^2 \} \\ &\quad - \frac{1}{2} \int d^3r \{ g_\omega \omega_0 - \frac{1}{2} c_3 \omega_0^4 \} \rho_v(r) - \frac{1}{2} \int d^3r A_0 \rho_c(r) - mA. \end{aligned} \quad (19)$$

Eq. (13) is solved self-consistently using the Runge-Kutta algorithm and the shooting method, and the Laplace equations, given by Eq. (15), are solved employing a Green Function method.

## B. Neutron stars

Next we discuss the RMF Lagrangian density used for describing a neutron star consisting of only nucleons and leptons (mainly electrons,  $e^-$ , and muons,  $\mu^-$ ). The Lagrangian density

associated with the leptons is:

$$\mathcal{L}_{lepton} = \sum_{\lambda=e^-, \mu^-} \bar{\psi}_\lambda (i\gamma^\mu \partial_\mu - m_\lambda) \psi_\lambda, \quad (20)$$

such that the full Lagrangian density under consideration consists of a hadronic part, given by Eq. (7), plus a leptonic part, given by Eq. (20). Introducing the mean field and no-sea approximations, the equations of motion for baryons and mesons can be derived. The detailed formalism of which can be found in Ref. [32]. The Dirac equation represents the equation of motion associated with the leptons. Based on chemical equilibrium and charge neutral conditions, for a given total baryon density, the equations of motion are solved self-consistently by iteration, and the meson fields, particle densities and Fermi momenta of each species (protons, neutrons, electrons, and muons) are obtained simultaneously.

The canonical energy-momentum tensor is derived by invoking the invariance of spacetime translation, namely:

$$T^{\mu\nu} = -g^{\mu\nu}\mathcal{L} + \sum_{\phi} \frac{\partial \mathcal{L}}{\partial(\partial_\mu \phi)} \partial^\nu \phi, \quad (21)$$

where  $g^{\mu\nu}$  is the Minkowski metric in rectilinear coordinates. For the case in which neutron star matter can be considered to be a perfect fluid, the energy-momentum tensor is given by [31]:

$$T^{\mu\nu} = \begin{pmatrix} \epsilon & 0 & 0 & 0 \\ 0 & p & 0 & 0 \\ 0 & 0 & p & 0 \\ 0 & 0 & 0 & p \end{pmatrix}. \quad (22)$$

Comparing the ground-state expectation value of Eq. (21) with Eq. (22), via the field equations the energy density,  $\epsilon$ , and the pressure,  $P$ , are given by:

$$\begin{aligned} \epsilon &= \frac{1}{2}m_\sigma^2\sigma^2 + \frac{1}{3}g_2\sigma^3 + \frac{1}{4}g_3\sigma^4 + \frac{1}{2}m_\omega^2\omega_0^2 + \frac{3}{4}c_3\omega_0^4 + \frac{1}{2}m_\rho^2\rho_{0,3}^2 + 12g_\rho^2g_\omega^2\Lambda_v\omega_0^2\rho_{0,3}^2 \\ &\quad + \frac{1}{\pi^2} \sum_{B=n,p} \int_0^{k_B} k^2 dk \sqrt{k^2 + (m_B + g_\sigma\sigma)^2} + \frac{1}{\pi^2} \sum_{\lambda=e^-, \mu^-} \int_0^{k_\lambda} k^2 dk \sqrt{k^2 + m_\lambda^2}, \end{aligned} \quad (23)$$

$$\begin{aligned} P &= -\frac{1}{2}m_\sigma^2\sigma^2 - \frac{1}{3}g_2\sigma^3 - \frac{1}{4}g_3\sigma^4 + \frac{1}{2}m_\omega^2\omega_0^2 + \frac{1}{4}c_3\omega_0^4 + \frac{1}{2}m_\rho^2\rho_{0,3}^2 + 4g_\rho^2g_\omega^2\Lambda_v\omega_0^2\rho_{0,3}^2 \\ &\quad + \frac{1}{3\pi^2} \sum_{B=n,p} \int_0^{k_B} \frac{k^4}{\sqrt{k^2 + (m_B + g_\sigma\sigma)^2}} dk + \frac{1}{3\pi^2} \sum_{\lambda=e^-, \mu^-} \int_0^{k_\lambda} dk \frac{k^4}{\sqrt{k^2 + m_\lambda^2}}, \end{aligned} \quad (24)$$

where  $k_B$  and  $k_\lambda$  are the Fermi momenta of baryons and leptons respectively.

The mass and radius of a neutron star are obtained by employing the Oppenheimer-Volkoff (OV) equations [33, 34]:

$$\frac{dp(r)}{dr} = -\frac{[p(r) + \epsilon(r)][M(r) + 4\pi r^3 p(r)]}{r(r - 2M(r))}, \quad (25)$$

$$M(r) = 4\pi \int_0^r \epsilon(r') r'^2 dr', \quad (26)$$

where  $r$  denotes the radial coordinate relative to the center of the star,  $p(r)$  and  $\epsilon(r)$  are the pressure and energy density at a radial point  $r$  in the star respectively, and  $M(r)$  represents the mass of the sphere contained within a radius  $r$ . Since zero pressure cannot support a neutron star from collapsing, we define the radius,  $R$ , of the star as that radius at which the pressure is zero. The mass total mass,  $M(R)$ , of the star is subsequently defined as the mass contained within a sphere of radius  $R$ .

### III. EXTRACTION OF PARAMETER SETS FOR NEW RMF MODELS

In this section we present the procedure and criteria for extracting values for our new coupling constants  $\Gamma_1$  and  $\Gamma_2$  in Eqs. (5) and (6) respectively. In particular, we consider the addition of these new isospin-dependent higher order correction terms to the PK1 [23], NL3 [24], S271 and Z271 [25] RMF models. The parameters sets for these interactions are presented in Table II.

We start with the recent PK1 effective interaction [23]. The PK1 effective interaction provides an excellent description of the properties of nuclear matter as well as for nuclei near and far from the valley of  $\beta$  stability. For this interaction, symmetric nuclear matter saturates at a Fermi momentum of  $1.30 \text{ fm}^{-1}$  with a binding energy per nucleon of  $-16.27 \text{ MeV}$  and an incompressibility of  $K = 283 \text{ MeV}$ . For comparison with the results of the PK1 effective interaction, we also employ the NL3, S271, and Z271 effective interactions, which have been used in Refs. [25, 27] to observe the effects of adding a nonlinear omega-rho coupling term, given by Eq. (4), on the neutron skin thickness,  $S$ , in  $^{208}\text{Pb}$  and the radius of 1.4 solar-mass neutron star. The NL3 effective interaction has also been used extensively to reproduce a variety of nuclear properties, such as binding energies, nuclear radii, nuclear density distribution, single particle spectra, etc. The NL3 and S271 effective interactions contain a sigma-meson self-coupling and Z271 includes both sigma- and omega-meson self-

couplings. These three interactions produce the following properties for symmetric nuclear matter: saturation at a Fermi momentum of  $1.30 \text{ fm}^{-1}$ , a binding energy per nucleon of  $-16.24 \text{ MeV}$ , and an incompressibility of  $K = 271 \text{ MeV}$ .

Later in this section we will discuss the procedure for calibrating values of the  $\Gamma_1$  and  $\Gamma_2$  couplings, in Eqs. (5) and (6), with respect to the symmetry energy, a quantity which we now briefly discuss. The energy of asymmetric nuclear matter can be expanded around the energy of symmetric nuclear matter – where symmetric nuclear matter is characterized by identical proton and neutron densities,  $\rho_p$  and  $\rho_n$  respectively – as:

$$\frac{E}{A}(\rho, t) = \frac{E}{A}(\rho, t=0) + t^2 a_{sym}(\rho) + O(t^4), \quad (27)$$

where  $\rho = \rho_n + \rho_p = \frac{2k_F^3}{3\pi^2}$ ,  $k_F$  is the the Fermi momentum,  $a_{sym}(\rho)$  is the symmetry energy, and the asymmetry,  $t$ , is defined as:

$$t \equiv \frac{\rho_n - \rho_p}{\rho_n + \rho_p}. \quad (28)$$

The symmetry energy,  $a_{sym}(\rho)$ , describes how the energy of asymmetric nuclear matter changes with the asymmetry,  $t$ . From Eq. (27), and employing Eq. (19), one can extract the following expression for the symmetry energy of nuclear matter in RMF:

$$a_{sym}(\rho) = \left( \frac{\partial^2 \frac{E}{A}(\rho, t)}{\partial t^2} \right)_{t=0} = \frac{k_F^2}{6E_F^*} + \frac{g_\rho^2}{12\pi^2} \frac{k_F^3}{m^{*2}}, \quad (29)$$

where  $E_F^{*2} = k_F^2 + m^{*2}$ ,  $m^* = m + g_\sigma\sigma$  is the effective nucleon mass, and the effective rho-meson mass,  $m_\rho^*$ , is defined as:

$$m_\rho^{*2} = \frac{m_\rho^2 + 8\Lambda_v g_\rho^2 g_\omega^2 \omega_0^2}{(1 + \Gamma_1 \frac{g_\sigma\sigma}{m} + \Gamma_2 (\frac{g_\sigma\sigma}{m})^2)^2}. \quad (30)$$

There are two terms in the symmetry energy. The first term in Eq. (29) represents the increase in the kinetic energy of the system when there is a relative displacement of the neutron and proton Fermi energies, and the second term in Eq. (29) represents the coupling between effective rho-meson and an isovector-vector current which no longer vanishes in asymmetric nuclear matter.

We now describe our procedure for extracting values of  $g_\rho$ ,  $\Lambda_v$ , and  $\Gamma_1$ , with  $\Gamma_2 = 0$ , in the Lagrangian density given by Eq. (7). The symmetry energy at saturation density, corresponding to  $k_f = 1.30 \text{ fm}^{-1}$ , is not well constrained by the binding energy of nuclei.

However, some average of the symmetry energy at full density and the surface energy is constrained by the binding energy [25]. We adopt the procedure of Horowitz and Piekarewicz, whereby we choose values of  $\Lambda_v$  and  $\Gamma_1$  with  $\Gamma_2 = 0$ , and then adjust the value  $g_\rho$  such that the effective interaction has a fixed symmetry energy at an average density of  $k_f = 1.15 \text{ fm}^{-1}$  ( $\rho = 0.10 \text{ fm}^{-3}$ ) and the binding energy per nucleon in  $^{208}\text{Pb}$  lies in the range  $|E/A - (E/A)_{exp}| \leq 0.005 \text{ MeV}$ , where  $(E/A)_{exp}$  represents the experimental value. The symmetry energy at  $k_f = 1.15 \text{ fm}^{-1}$  is 26.08 MeV for the original PK1 effective interaction and 25.68 MeV for the original NL3, S271, and Z271 effective interactions, respectively. A similar procedure is followed for extracting parameter values for  $g_\rho$ ,  $\Lambda_v$ , and  $\Gamma_2$ , with  $\Gamma_1 = 0$ .

The experimental binding energy per nucleon,  $(E/A)_{exp}$ , in  $^{208}\text{Pb}$  is  $-7.868 \text{ MeV}$  [35]. As the correction for center of mass motion is neglected in the self-consistent RMF calculation, for comparative purposes an “equivalent” experimental  $(E/A)_{exp} = -7.843 \text{ MeV}$  for  $^{208}\text{Pb}$  is used instead, which is estimated via the harmonic oscillator phenomenological formula  $E_{cm} = 0.75 \hbar\omega_0$  with  $\hbar\omega_0 = 41A^{-1/3}$  [13].

To avoid abnormal solutions at zero density for nuclear matter,  $\Lambda_v$  in Eq. (4) should not be negative. However, there is no such constraint on the values of  $\Gamma_1$  and  $\Gamma_2$  in Eqs. (5) and (6) respectively. The role of the  $\Gamma_1$ ,  $\Gamma_2$  and  $\Lambda_v$  couplings is to modify the density dependence of the symmetry energy. In Fig. 1, we see that increasing  $\Gamma_1$ , decreasing  $\Gamma_2$ , or increasing  $\Lambda_v$  (see Ref. [27]), causes the symmetry energy to grow more slowly with density.

After readjusting the coupling constant  $g_\rho$ , we perform self-consistent calculations as stated in Sec. II to determine the properties of  $^{208}\text{Pb}$  and a 1.4 solar-mass neutron star. The numerical values of different combinations of  $\Lambda_v$ ,  $\Gamma_1$  (or  $\Gamma_2$ ) and  $g_\rho$ , and the corresponding binding energy per nucleon,  $E/A$ , the proton root mean square radius,  $R_p$ , the neutron skin thickness,  $S$ , and the radius,  $R$ , of a 1.4 solar-mass neutron star, are also listed in Tables III to VIII.

## IV. RESULTS AND DISCUSSION

### A. Neutron radius of $^{208}\text{Pb}$

In this section we study the sensitivity of the neutron skin thickness,  $S$ , in  $^{208}\text{Pb}$  with respect to the addition of two new terms, given by Eqs (5) and (6), to the original Lagrangian

densities for each of the PK1, NL3, S271 and Z271 effective interactions. In particular we also extract values of the neutron rms radius for RMF parameter sets which are consistent with experimental binding energies as well as with the properties of nuclear matter specified in the previous section.

We start by considering the PK1 effective interaction and study the effect of different combinations of  $\Lambda_v$  and  $\Gamma_1$ , with  $\Gamma_2 = 0$ , as well as different combinations of  $\Lambda_v$  and  $\Gamma_1$ , with  $\Gamma_2 = 0$  – in the total Lagrangian density given by Eq. (7) – on the neutron skin thickness, neutron and proton rms radii, as well as neutron and proton density distributions. In order to understand the role of various coupling constants, we initially focus on the special case where  $\Gamma_2 = 0$  and consider the effect of different combinations of  $\Lambda_v$  and  $\Gamma_1$ , which are chosen according to the procedure outlined in Sec. III. The value of  $g_\rho$  is always chosen so as to reproduce the symmetry energy at an average density of  $k_f = 1.15 \text{ fm}^{-1}$  corresponding to  $a_{asm} = 26.08 \text{ MeV}$ . In Fig. 2, the binding energy per nucleon,  $E/A$ , versus the neutron skin thickness,  $S$ , is presented. Different lines correspond to results with different  $\Gamma_1$  for fixed values of  $\Lambda_v$  as indicated in the figure. The direction of the arrow next to the various lines corresponds to increasing values of  $\Gamma_1$ . The open circles are the results for  $\Gamma_1 = 0$ . The symbols retain their meanings in similar figures to follow. The effect of increasing  $\Gamma_1$  is to decrease  $S$ , while decreasing the absolute value of the binding energy. With the additional constraint that the experimental binding energy per nucleon,  $(E/A)_{exp}$ , is  $-7.843 \text{ MeV}$  (indicated by the dashed line in Fig. 2), one can extract values of  $S$  which range from 0.159 to 0.277 fm for different combinations of  $\Gamma_1$  and  $\Lambda_v$ . More detailed results are listed in Table III.

The accurately measured value of the proton rms radius,  $R_p$ , of  $^{208}\text{Pb}$ , namely  $5.45 \pm 0.02 \text{ fm}$  [12], places a stringent constraint on the choice of coupling constants. In Fig. 3, we also display the neutron and proton rms radii as functions of different combinations of  $\Lambda_v$  and  $\Gamma_1$ , with  $\Gamma_2 = 0$ . It is seen that the neutron rms radius is sensitive to different combinations of  $\Gamma_1$  and  $\Lambda_v$ , whereas the proton rms radius is insensitive and in good agreement with the experimental value. In Fig. 4, the neutron and proton density distributions have been computed for five different  $\Lambda_v$  and  $\Gamma_1$  combinations, which reproduce the experimental binding energy per nucleon for  $^{208}\text{Pb}$ . While combinations of  $\Lambda_v$  and  $\Gamma_1$  with small values of  $S$  tolerate larger neutron central densities, the proton density distributions essentially remain unchanged in all cases.

Next, we consider the PK1 effective interaction and study the effect of different combinations of  $\Lambda_v$  and  $\Gamma_2$ , for  $\Gamma_1 = 0$ , on  $S$ . The binding energy per nucleon,  $E/A$ , versus  $S$  is shown in Fig. 5. The symbols retain the same meanings as in Fig. 2, except that the roles of  $\Gamma_2$  and  $\Gamma_1$  are exchanged. Constraining the values of  $S$  via the experimental binding energy per nucleon, yields essentially the same range of values for  $S$  as was obtained in Fig. 2. The main difference between Figs. 2 and 5 lies in the fact that the values of  $\Gamma_2$  are negative and the absolute values thereof are larger than  $\Gamma_1$  for fixed values of  $\Lambda_v$ , and for the same values of the neutron skin thickness. More detailed results for different  $\Gamma_2$  and  $\Lambda_v$  combinations are listed in Table IV. Once again, we mention the fact that the proton rms radius is well constrained by the experimental data.

Previous RMF models predicted values of  $S$  in  $^{208}\text{Pb}$  which ranged from 0.2 to 0.3 fm [9, 11]. In our present analysis, we obtain values of  $S$  ranging from 0.159 to 0.277 fm, for different  $\Lambda_v$  and  $\Gamma_1$  (or  $\Gamma_2$ ) combinations for the PK1 effective interaction, with the binding energy and proton rms radius both constrained by data. More specifically, our new models yield a minimum value of  $S = 0.159$  fm for  $\Lambda_v = 0.035$  and  $\Gamma_1 = 0.2$  (or  $\Gamma_2 = -0.55$ ) in comparison with  $S = 0.16 \pm 0.02$  fm given by modern Skryme Hartree-Fock models [10].

We now repeat the above analysis for the NL3 effective interaction. In Fig. 6, the binding energy per nucleon,  $E/A$ , versus  $S$  is shown for different combinations of (a)  $\Lambda_v$  and  $\Gamma_1$  (left panel), with  $\Gamma_2 = 0$ , and (b) for different combinations of  $\Lambda_v$  and  $\Gamma_2$  (right panel), with  $\Gamma_1 = 0$ . Constraining the values of  $S$  via the experimental binding energy per nucleon, yields a range of values for  $S$  similar to those associated with the PK1 effective interaction. The minimum value of  $S$  is 0.155 fm and this corresponds to the  $\Lambda_v = 0.035$  and  $\Gamma_1 = 0.25$ , with  $\Gamma_2 = 0$ , combination. More detailed data regarding the parameter sets and associated observables are listed in Tables V and VI.

Next, we study the effect of adding our new terms on two additional effective interactions, namely the S271 and Z271 parameterizations of RMF [25, 27]. The original parameters for these interactions were extracted by fitting to the properties of nuclear matter and the experimentally determined proton radius of  $^{208}\text{Pb}$ . The addition of the  $\Lambda_v$  term, given by Eq. (4), to the Lagrangian Eq. (1), reduces the values of the neutron skin thickness in  $^{208}\text{Pb}$  for both the S271 and Z271 effective interactions, while sacrificing good fits to the experimental binding energy per nucleon. The latter was the result of Ref. [27], the points of which are indicated by open circles in Fig. 7. The effect of different combinations [in the

Lagrangian given by Eq. (7)] of  $\Lambda_v$  and  $\Gamma_1$ , with  $\Gamma_2 = 0$ , and various combinations of  $\Lambda_v$  and  $\Gamma_2$ , with  $\Gamma_1 = 0$ , on  $S$  is displayed in the different panels in Fig. 7. Constraining the values of  $S$  via the experimental binding energy per nucleon for the S271 effective interaction (see upper panels in Fig. 7), yields values of  $S$  which range from 0.106 to 0.258 fm, for different combinations of  $\Gamma_1$  ( $\Gamma_2$ ) and  $\Lambda_v$ . A slight narrower range is obtained for the Z271 effective interaction, namely  $S = 0.134 \sim 0.241$  fm: see lower panels in Fig. 6. The main difference between the S271 and Z271 effective interactions is that the signs of  $\Gamma_1$  and  $\Gamma_2$  are opposite at points corresponding to the experimental binding energy per nucleon. More detailed data on  $S$  versus the binding energy per nucleon for different  $\Gamma_1$  and  $\Lambda_v$  combinations for S271 and Z271 are presented in Tables VII and VIII. As is the case with the PK1 and NL3 effective interactions, we have checked that the proton rms radius of  $^{208}\text{Pb}$  agrees well with the experimental data.

Previously it has been demonstrated that, for the original RMF models of interest to this paper, a linear relationship exists between the neutron skin thickness for  $^{208}\text{Pb}$  and symmetry energy of nuclear matter at saturation density [10, 11, 26]. After the inclusion of our new terms, given by Eqs. (5) and (6), we study this relation for each of PK1, NL3, S271 and Z271 effective interactions: the results are presented in Fig. 8. For this study we only take combinations of  $\Lambda_v$  and  $\Gamma_1$  ( $\Gamma_2$ ) which reproduce both the experimental binding energy as well as the experimental proton rms radius of  $^{208}\text{Pb}$ . Indeed, we also observe a linear relation between the neutron skin thickness,  $S$  (in fm), and the nuclear symmetry energy,  $a_{sym}$  (in MeV), which can be expressed as:

$$S \approx -0.283 + 0.015 a_{sym}. \quad (31)$$

At the saturation point, the symmetry energy,  $a_{sym}$ , for the various interactions, ranges from 29 to 38 MeV and the neutron skin thickness,  $S$ , ranges from 0.14 to 0.28 fm.

The addition of our new higher order correction terms, expressed via Eqs. (5) and (6), to existing RMF models can be associated with some kind of multi-meson exchange processes occurring in the inner (higher density) region of nuclei. In low-energy nucleon-nucleon scattering models, the exchange of mesons with an effective mass of less than 1 GeV seems to be the dominant contribution to the scattering amplitudes. After one-meson exchange, the inclusion of two-meson exchange at low energies has been demonstrated to provide a major improvement in the theoretical description of nucleon-nucleon scattering data [22]. In the

inner region of a heavy nucleus such as  $^{208}\text{Pb}$ , one could imagine that multi-meson exchange processes, expressed via Eqs. (5) and (6), could play an important role in modifying the short range behaviour of the nucleon-nucleon interaction, by softening the density dependence of the symmetry energy at high density (the inner part of nuclei) and thus leading to smaller values of neutron skin thickness  $S$  compared to previous interactions which excluded our new correction terms.

In principle one could include the isospin-dependent nuclear force associated with the long-range pseudoscalar pion. However, because of parity conservation, the pion cannot contribute in a mean-field treatment of the ground state of spherical nuclei as  $^{208}\text{Pb}$ . Moreover, what determines the neutron skin thickness seems to be the neutron distribution in the inner core of nuclei, which in turn is more sensitive to the short-range part of the nuclear force. The above arguments suggest that pion contributions do not play an important role in determining the neutron skin thickness in  $^{208}\text{Pb}$ .

Since the parity-violating electron scattering experiment at Jefferson Lab can only provide information about the neutron radius, and hence also  $S$ , in  $^{208}\text{Pb}$ , it is also important to study the consequences of an exact measurement of  $S$  on other properties of this nucleus. In particular, we now observe the influence of different  $\Gamma_1$  ( $\Gamma_2$ ) and  $\Lambda_v$  combinations (which reproduce both the experimental binding energy as well as the experimental proton rms radius of  $^{208}\text{Pb}$ ), for both PK1 and NL3 effective interactions, to neutron single particle energy levels versus their corresponding neutron rms radii in  $^{208}\text{Pb}$ : the results are displayed in Fig. 9. We only consider the PK1 and NL3 effective interactions since they have been used to provide an excellent description of nuclei near and far from the valley of  $\beta$  stability. First we consider the original PK1 effective interaction ( $\Lambda_v = \Gamma_1 = \Gamma_2 = 0$ ) which yields  $S = 0.277$  fm. The corresponding neutron single particle energy levels are denoted by filled circles in the left panel of Fig. 9. We now compare these single particle energy levels to the values corresponding to those combinations of  $\Lambda_v$  and  $\Gamma_1$ , with  $\Gamma_2 = 0$ , and  $\Lambda_v$  and  $\Gamma_2$ , with  $\Gamma_1 = 0$ , which yield a minimum value for  $S$ . In particular, the combination of  $\Lambda_v = 0.035$  and  $\Gamma_1 = 0.2$ , with  $\Gamma_2 = 0$ , yields a minimum value of  $S = 0.159$  fm for the PK1 effective interaction and the corresponding single particle energy levels are denoted by open squares in Fig. 9. Also the combination of  $\Lambda_v = 0.035$  and  $\Gamma_2 = -0.55$ , with  $\Gamma_1 = 0$ , yields a minimum value of  $S = 0.159$  fm: the corresponding single particle energy levels are denoted by open triangles in Fig. 9. The quantum numbers associated with each of the levels are the same as those

associated with usual RMF predictions: see for example Ref. [23]. The effect of decreasing  $S$  is to deepen each single particle energy level and to decrease the corresponding neutron rms radius. More specifically, we see the addition of our new higher order correction terms is to deepen the deep-lying states more than the low-lying states. This, in turn, suggests the possibility that the effect of these new terms is to modify the short range behavior of the nucleon-nucleon interaction. In the right panel of Fig. 9, we observe the effect of adding our new terms on the neutron single particle energy levels and their corresponding neutron rms radii for the NL3 effective interaction: the results and discussion are similar to those associated with the PK1 effective interaction.

### B. Correlation between neutron skin thickness and the radius of a neutron star

We now discuss the effect of our new terms, given by Eqs. (5) and (6), on the radius,  $R$ , of a 1.4 solar-mass neutron star and also study its correlation with the neutron skin thickness,  $S$ , in  $^{208}\text{Pb}$  for the PK1, NL3, S271 and Z271 effective interactions. In particular, we consider the following combinations of parameters: (1)  $\Lambda_v$ ,  $\Gamma_1$  and  $\Gamma_2$  terms separately, (2)  $\Lambda_v$  and  $\Gamma_1$  terms, with  $\Gamma_2 = 0$ , and (3)  $\Lambda_v$  and  $\Gamma_2$  terms, with  $\Gamma_1 = 0$ .

After adding the  $\Lambda_v$  term, given by Eq. (4), to the Lagrangian given by Eq. (1), the relationship between  $R$  and  $S$  is displayed in Fig. 10: different line types correspond to different interactions. For all the interactions, values of  $R$  increase with increasing values of  $S$ . However, different interactions give different values of  $R$  for the same value of  $S$ . For example, for  $S = 0.21$  fm, values of  $R$  vary from 13.27 km for the NL3 effective interaction to 11.63 km for the Z271 effective interaction. Therefore, the radius of a 1.4 solar-mass neutron star is not uniquely constrained by a measurement of the neutron skin thickness, as has already been pointed out by Horowitz and Piekarewicz [27]. The reason for this is that  $S$  depends on the equation of state (EOS) near or below saturation density where most RMF models are calibrated to successfully describe the properties of nuclear matter and finite nuclei, whereas the neutron star radius is mainly sensitive to the EOS for higher densities. Hence, different RMF models give different predictions for the properties of neutron stars, and as such one cannot expect to reliably extrapolate any of these models to extreme conditions of isospin and density. However, combining separate measurements of  $S$  and  $R$  can provide valuable information on the EOS at low and high densities. For example, relatively large values of  $S$

suggest a stiff low-density EOS, while relatively small values of  $R$  imply a soft high density EOS, and vice versa.

In Fig. 11, we observe the effect of the  $\Gamma_1$  term, given by Eq. (5), with  $\Lambda_v = \Gamma_2 = 0$ , on the correlation between  $S$  and  $R$ . As expected,  $R$  increases with an increasing  $S$ , and different models give different relationships between  $R$  and  $S$ . The results for the PK1 and NL3 effective interactions are generally similar, but the value of  $R$  given by PK1 is smaller than that of NL3 for the same value of  $S$ . The S271 and Z271 effective interactions produce smaller neutron skin thicknesses, and also  $R$  increases more rapidly with  $S$  compared to PK1 and NL3. For example, for  $\Gamma_1 = 0$ ,  $S \simeq 0.280, 0.278, 0.254, 0.241$  fm, and the corresponding values of  $R$  are 14.08, 13.89, 13.62, 13.07 km for the NL3, PK1, S271 and Z271 effective interactions, respectively. As the value of  $\Gamma_1$  is increased to 1.0, the neutron skin thickness decreases to 0.252, 0.253, 0.240, 0.236 fm, and the corresponding values of  $R$  decrease to 13.01, 12.74, 12.50, 11.97 km for the NL3, PK1, S271 and Z271 effective interactions, respectively.

In Fig. 12, we observe the effect of the  $\Gamma_2$  term, given by Eq. (6), with  $\Lambda_v = \Gamma_1 = 0$ , on the correlation between  $S$  and  $R$ : the results and discussion are very similar to those associated with Fig. 11.

The effect of different combinations of  $\Lambda_v$  with  $\Gamma_1$ , with  $\Gamma_2 = 0$ , and  $\Lambda_v$  with  $\Gamma_2$ , with  $\Gamma_1 = 0$ , on the correlation between  $S$  and  $R$  for the (a) PK1, (b) NL3, (c) S271 and (d) Z271 effective interactions is displayed in Fig. 13. It is clear that the  $\Lambda_v$  term, given by Eq. (4), plays the most prominent role for decreasing the values of  $R$  and  $S$ , i.e. the  $\Lambda_v$  term has the largest effect on changing values of  $R$  and  $S$ . In the upper left panel, associated with the PK1 effective interaction, the minimum neutron skin thickness in  $^{208}\text{Pb}$  is  $S = 0.151$  fm for the combination  $\Lambda_v = 0.02$ ,  $\Gamma_1 = 0.8$ , and  $\Gamma_2 = 0.0$ , while the minimum radius of a 1.4 solar-mass neutron star is as low as  $R = 12.58$  km when  $\Lambda_v = 0.01$ ,  $\Gamma_1 = 1.0$ , and  $\Gamma_2 = 0.0$ . The corresponding results for the NL3, S271, and Z271 effective interactions are shown in the other panels in Fig. 13. The lowest value of the neutron skin thickness in  $^{208}\text{Pb}$  is  $S = 0.136$  fm for the S271 effective interaction with  $\Lambda_v = 0.05$ ,  $\Gamma_1 = 0.0$ , and  $\Gamma_2 = -2.0$ , and the smallest value of  $R$  is 11.28 km for Z271 with  $\Lambda_v = 0.1$ ,  $\Gamma_1 = 0.0$ , and  $\Gamma_2 = 0.0$ .

## V. SUMMARY

After introducing higher-order nucleon-sigma-rho coupling corrections to existing RMF models, and calibrating the various coupling constants with respect to the properties of nuclear matter, we observe a new range of values for the neutron skin thickness,  $S$ , in  $^{208}\text{Pb}$ , namely  $0.16 \sim 0.28$  fm for the PK1 and NL3 effective interactions and  $0.11 \sim 0.26$  fm for the S271 and Z271 effective interactions. This means that, on one hand, for some particular effective interactions (S271 and Z271) it is possible to obtain values of the neutron radius in the same range as those for nonrelativistic mean field models, while on the other hand, for other effective interactions (PK1 and NL3) the neutron skin thickness is slightly extended compared to the previous upper limit of 0.2 fm.

The addition of our new terms also has the effect of softening the density dependence of the symmetry energy at high densities. We also observe a linear relation between the neutron skin thickness and the nuclear symmetry energy at the saturation point.

We have extrapolated our new relativistic mean field models from normal to dense neutron matter so as to correlate the radius of a 1.4 solar-mass neutron star with the neutron skin thickness in  $^{208}\text{Pb}$ . We observe that the radius of a 1.4 solar-mass neutron star is not uniquely constrained by a measurement of the neutron skin thickness and is also model-dependent.

### Acknowledgments

This work is partly supported by the Major State Basic Research Development Program Under Contract Number G2000077407, the National Natural Science Foundation of China under Grant No. 10025522 and 10221003, as well as the National Research Foundation of South Africa under Grant No. 2054166. GCH also acknowledges invaluable discussions with Chuck Horowitz, from Indiana University in Bloomington, Indiana USA, which served as the original catalyst for this project.

- 
- [1] E. N. Fortson, Y. Pang, and L. Wilets, Phys. Rev. Lett. **65**, 2857 (1990).
  - [2] B. W. Allardice, C. J. Batty, D. J. Baugh, E. Friedman, G. Heymann, M. E. Cage, G. J. Pyle, G. T. A. Squier, A. S. Clough, D. F. Jackson, S. Murugesu, and V. Rajaratnam, Nucl. Phys.

A **209**, 1 (1973).

- [3] V. E. Starodubsky and N. M. Hintz, Phys. Rev. C **49**, 2118(1994).
- [4] A. Krasznahorkay, A. Balandz, J. A. Bordewijk, S. Brandenburg, M. N. Harakeh, N. Kalantar-Nayestanaki, B. N. Nyak, J. Timr, and A. van der Woude, Nucl. Phys. A **567**, 521(1994).
- [5] S. Karataglidis , K. Amos, B. A. Brown, and P. K. Deb, Phys. Rev. C **65**, 044306 (2002).
- [6] B. C. Clark, L. J. Kerr, and S. Hama, Phys. Rev. C **67**, 054605 (2003).
- [7] A. Trzcińska, J. Jastrzeski, P. Lubiński F. J. Hartmann, R. Schmidt, T. von Egidy, and B. Kłos, Phys. Rev. Lett. **87**, 082501 (2002).
- [8] Jefferson Laboratory Experiment E-00-003, Spokespersons R. Michaels, P. A. Souder, and G. M. Urciuoli.
- [9] S. Typel and B. A. Brown, Phys. Rev. C **64**, 027302 (2001).
- [10] B. A. Brown, Phys. Rev. Lett. **85**, 5296 (2000).
- [11] R. J. Furnstahl, Nucl. Phys. A **706**, 85 (2002).
- [12] G. Fricke, C. Bernhardt, K. Heilig, L. A. Schaller, L. Schellenberg, E. B. Shera, and C. W. De Jager, At. Data Nucl. Data Tables **60**, 177 (1995).
- [13] J. Meng, Nucl. Phys. A **635**, 3 (1998); J. Meng and P. Ring, Phys. Rev. Lett. **77**, 3963 (1996).
- [14] J. Meng and P. Ring, Phys. Rev. Lett. **80**, 460 (1998).
- [15] J. Meng, I. Tanihata, and S. Yamaji, Phys. Lett. B **419**, 1 (1998).
- [16] J. Meng, S. G. Zhou, and I. Tanihata, Phys. Lett. B **532**, 209 (2002).
- [17] J. Meng, H. Toki, J. Y. Zeng, S. Q. Zhang, and S. G. Zhou, Phys. Rev. C **65**, 041302 (2002).
- [18] J. N. Ginocchio, Phys. Rev. Lett. **78**, 436 (1997).
- [19] J. Meng, K. Sugawara-Tanabe, S. Yamaji, P. Ring, and A. Arima, Phys. Rev. C **58**, R628 (1998).
- [20] J. Meng and I. Tanihata, Nucl.Phys. A **650**, 176-196 (1999).
- [21] J. Meng, K. Sugawara-Tanabe, S. Yamaji, and A. Arima, Phys. Rev. C **59**, 154 (1999).
- [22] Th. A. Rijken and V. G. J. Stoks, Phys. Rev. C **54**, 2851 (1996).
- [23] W. H. Long, J. Meng, N. Van Giai, and S. G. Zhou, Phys. Rev. C **69**, 034319 (2004).
- [24] G. A. Lalazissis, J. König, and P. Ring, Phys. Rev. C **55**, 540 (1997).
- [25] C. J. Horowitz and J. Piekarewicz, Phys. Rev. Lett. **86**, 5647 (2001).
- [26] A. E. L. Dieperink, Y. Dewulf, D. Van Neck, M. Waroquier, and V. Rodin, Phys. Rev. C **68**, 064307 (2003).

- [27] J. Carriere, C. J. Horowitz, and J. Piekarewicz, *Astrophys. J.* **593**, 463 (2003).
- [28] B. D. Serot and J. D. Walecka, *Adv. Nucl. Phys.* **16**, 1 (1986).
- [29] P.-G. Reinhard, *Rep. Prog. Phys.* **52**, 439 (1989).
- [30] P. Ring, *Prog. Part. Nucl. Phys.* **37**, 193 (1996).
- [31] N. K. Glendenning, *Compact Stars*, (Springer-Verlag, New York, 2000).
- [32] S. F. Ban, J. Li, S. Q. Zhang, H. Y. Jia, J. P. Sang, and J. Meng, *Phys. Rev. C* **69**, 045805 (2004).
- [33] J. R. Oppenheimer and G. M. Volkoff, *Phys. Rev.* **55**, 374 (1939).
- [34] R. C. Tolman, *Phys. Rev.* **55**, 364 (1939).
- [35] G. Audi, O. Bersillon, J. Blachot, and A. H. Wapstra, *Nucl. Phys. A* **624**, 1-124 (1997).

TABLE I: Summary of current values for the neutron skin thickness,  $S$ , in  $^{208}\text{Pb}$ 

Probe	$S$ (fm)	Error (fm)	Reference
$\pi^+$ and $\pi^-$ scattering	0.0	0.1	[2]
Proton scattering (650 MeV)	0.20	0.04	[3]
Giant dipole resonance excitation	0.19	0.09	[4]
Nucleon scattering (40 - 200 MeV)	0.17		[5]
Proton-nucleus scattering (0.5-1.04 GeV)	0.097	0.014	[6]
Anti-protonic atoms	0.15	0.02	[7]

TABLE II: Parameter sets associated with the original PK1, NL3, S271, and Z271 RMF models. The nucleon and rho meson masses are kept fixed at  $M = 939$  MeV for both protons,  $p$ , and neutrons,  $n$ , and  $m_\rho = 763$  MeV for the NL3, S271, and Z271 effective interactions. For the PK1 effective interaction,  $M_n = 939.5731$  MeV,  $M_p = 938.2796$  MeV and  $m_\rho = 763$  MeV.

RMF model	$g_\sigma$	$g_\omega$	$g_2$ (fm $^{-1}$ )	$g_3$	$c_3$	$m_\sigma$ (MeV)	$m_\omega$ (MeV)
PK1	10.3222	13.0131	-8.1688	-9.9976	55.636	514.0819	784.254
NL3	10.217	12.868	-10.431	-28.885	0	508.194	782.5
S271	9.006	10.806	-12.37	-17.323	0	505	783
Z271	7.031	8.406	-5.435	63.691	49.941	465	783

TABLE III: Results for the PK1 effective interaction with  $\Gamma_2 = 0$ . For each  $\Lambda_v$ , the range of  $\Gamma_1$  is given with the corresponding  $g_\rho$  coupling constant. Also listed are the binding energy per nucleon,  $E/A$ , the proton root mean square radius,  $R_p$ , the neutron skin thickness,  $S$ , in  $^{208}\text{Pb}$ , and the radius,  $R$ , of a 1.4 solar-mass neutron star.

$\Lambda_v$	$\Gamma_1$	$4g_\rho^2$	$E/A$ (MeV)	$R_p$ (fm)	$S$ (fm)	$R$ (km)
0.005	0.00000	87.75942	-7.85382	5.44398	0.26332	13.5650
	0.05000	90.55426	-7.84285	5.44407	0.26224	13.4509
0.01	0.00000	93.54758	-7.86507	5.44561	0.24868	13.3450
	0.10000	100.40040	-7.84225	5.44608	0.24558	13.2510
0.015	0.00000	101.28410	-7.87067	5.44764	0.23500	13.1970
	0.15000	113.12450	-7.83869	5.44906	0.22817	13.0560
0.02	0.00000	109.87232	-7.87696	5.45031	0.22105	13.0880
	0.15000	123.96595	-7.84521	5.45239	0.21255	12.9596
0.025	0.00000	120.07776	-7.88201	5.45351	0.20705	13.0080
	0.20000	143.71214	-7.83903	5.45747	0.19295	12.8760
0.03	0.00000	132.38804	-7.88579	5.45726	0.19285	12.9440
	0.20000	161.69666	-7.84229	5.46243	0.17613	12.8290
0.035	0.00000	147.51000	-7.88824	5.46158	0.17828	12.8950
	0.20000	184.83000	-7.84363	5.46817	0.15861	12.7910

TABLE IV: Results for the PK1 effective interaction with  $\Gamma_1 = 0$ . For each  $\Lambda_v$ , the range of  $\Gamma_2$  is given with the corresponding  $g_\rho$  coupling constant. Also listed are the binding energy per nucleon,  $E/A$ , the proton root mean square radius,  $R_p$ , the neutron skin thickness,  $S$ , in  $^{208}\text{Pb}$ , and the radius,  $R$ , of a 1.4 solar-mass neutron star.

$\Lambda_v$	$\Gamma_2$	$4g_\rho^2$	$E/A$ (MeV)	$R_p$ (fm)	$S$ (fm)	$R$ (km)
0.005	0.00000	87.75942	-7.85382	5.44398	0.26332	13.5650
	-0.10000	89.34030	-7.84601	5.44358	0.26214	13.4870
0.01	0.00000	93.54758	-7.86507	5.44561	0.24868	13.3450
	-0.30000	99.48068	-7.84046	5.44480	0.24426	13.1470
0.015	0.00000	101.28410	-7.87067	5.44764	0.23500	13.1970
	-0.30000	107.86900	-7.84779	5.44734	0.22936	13.0240
0.02	0.00000	109.87232	-7.87696	5.45031	0.22105	13.0880
	-0.40000	120.51648	-7.84641	5.45060	0.21207	12.8950
0.025	0.00000	120.07776	-7.88201	5.45351	0.20705	13.0080
	-0.50000	136.42240	-7.84380	5.45487	0.19386	12.7980
0.03	0.00000	132.38804	-7.88579	5.45726	0.19285	12.9440
	-0.60000	157.20144	-7.83931	5.46024	0.17446	12.7290
0.035	0.00000	147.51000	-7.88824	5.46158	0.17828	12.8950
	-0.55000	175.83000	-7.84514	5.46548	0.15931	12.7150

TABLE V: Results for the NL3 effective interaction with  $\Gamma_2 = 0$ . For each  $\Lambda_v$ , the range of  $\Gamma_1$  is given with the corresponding  $g_\rho$  coupling constant. Also listed are the binding energy per nucleon,  $E/A$ , the proton root mean square radius,  $R_p$ , the neutron skin thickness,  $S$ , in  $^{208}\text{Pb}$ , and the radius,  $R$ , of a 1.4 solar-mass neutron star.

$\Lambda_v$	$\Gamma_1$	$4g_\rho^2$	$E/A$ (MeV)	$R_p$ (fm)	$S$ (fm)	$R$ (km)
0.005	0.00000	84.86094	-7.86252	5.46039	0.26546	13.7800
	0.10000	90.36404	-7.84141	5.46047	0.26303	13.6790
0.01	0.00000	90.85902	-7.87088	5.46146	0.25128	13.5790
	0.15000	100.68116	-7.83939	5.46208	0.24585	13.4440
0.015	0.00000	97.85166	-7.87783	5.46320	0.23729	13.4390
	0.15000	109.28612	-7.84707	5.46441	0.23016	13.3270
0.02	0.00000	105.92526	-7.88395	5.46557	0.22333	13.3430
	0.20000	124.63490	-7.84268	5.46822	0.21123	13.2090
0.025	0.00000	115.51950	-7.88873	5.46853	0.20935	13.2670
	0.20000	138.10950	-7.84746	5.47226	0.19486	13.1530
0.03	0.00000	127.01290	-7.89232	5.47206	0.19521	13.2110
	0.25000	163.48180	-7.83926	0.17318	5.47856	13.0601
0.035	0.00000	141.00000	-7.89472	5.47619	0.18076	13.1630
	0.25000	187.42000	-7.84020	5.48457	0.15495	13.0500

TABLE VI: Results for the NL3 effective interaction with  $\Gamma_1 = 0$ . For each  $\Lambda_v$ , the range of  $\Gamma_2$  is given with the corresponding  $g_\rho$  coupling constant. Also listed are the binding energy per nucleon,  $E/A$ , the proton root mean square radius,  $R_p$ , the neutron skin thickness,  $S$ , in  $^{208}\text{Pb}$ , and the radius,  $R$ , of a 1.4 solar-mass neutron star.

$\Lambda_v$	$\Gamma_2$	$4g_\rho^2$	$E/A$ (MeV)	$R_p$ (fm)	$S$ (fm)	$R$ (km)
0.005	0.00000	84.86094	-7.86252	5.46039	0.26546	13.7800
	-0.30000	89.60516	-7.83969	5.45879	0.26154	13.5590
0.01	0.00000	90.85902	-7.87088	5.46146	0.25128	13.5790
	-0.40000	98.28740	-7.84082	5.45993	0.24456	13.3320
0.015	0.00000	97.85166	-7.87783	5.46320	0.23729	13.4390
	-0.50000	108.86836	-7.84069	5.46217	0.22699	13.1880
0.02	0.00000	105.92526	-7.88395	5.46557	0.22333	13.3430
	-0.60000	121.92576	-7.83948	5.46551	0.20865	13.0860
0.025	0.00000	115.51950	-7.88873	5.46853	0.20935	13.2670
	-0.60000	134.79210	-7.84435	5.46965	0.19256	13.0470
0.03	0.00000	127.01290	-7.89232	5.47206	0.19521	13.2110
	-0.70000	155.35130	-7.83993	5.47508	0.17258	12.9820
0.035	0.00000	141.00000	-7.89472	5.47619	0.18076	13.1630
	-0.65000	173.66000	-7.84539	5.48046	0.15725	12.9770

TABLE VII: Results for the S271 effective interaction with  $\Gamma_2 = 0$ . For each  $\Lambda_v$ , the range of  $\Gamma_1$  is given with the corresponding  $g_\rho$  coupling constant. Also listed are the binding energy per nucleon,  $E/A$ , the proton root mean square radius,  $R_p$ , the neutron skin thickness,  $S$ , in  $^{208}\text{Pb}$ , and the radius,  $R$ , of a 1.4 solar-mass neutron star.

$\Lambda_v$	$\Gamma_1$	$4g_\rho^2$	$E/A$ (MeV)	$R_p$ (fm)	$S$ (fm)	$R$ (km)
0.01	0.00000	91.58490	-7.94895	5.45986	0.23786	13.0880
	0.55000	121.352251	-7.84226	5.46037	0.22586	12.5867
0.02	0.00000	98.52548	-7.96073	5.46078	0.22151	12.7970
	0.65000	141.943385	-7.83858	5.46372	0.19862	12.3605
0.03	0.00000	106.66758	-7.97100	5.46247	0.20543	12.6290
	0.70000	165.27674	-7.84191	5.46869	0.17193	12.2640
0.04	0.00000	116.33780	-7.97978	5.46487	0.18950	12.5210
	0.75000	197.6836	-7.84262	5.47557	0.14352	12.3314
0.05	0.00000	127.87086	-7.98742	5.46795	0.17358	12.4470
	0.80000	245.799698	-7.83967	5.48465	0.11255	-

TABLE VIII: Results for the Z271 effective interaction with  $\Gamma_2 = 0$ . For each  $\Lambda_v$ , the range of  $\Gamma_1$  is given with corresponding coupling constant  $g_\rho$  between rho meson and nucleon. Also listed are the binding energy per nucleon,  $E/A$ , the proton root mean square radius,  $R_p$ , the neutron skin thickness,  $S$ , in  $^{208}\text{Pb}$ , and the radius,  $R$ , of a 1.4 solar-mass neutron star.

$\Lambda_v$	$\Gamma_1$	$4g_\rho^2$	$E/A$ (MeV)	$R_p$ (fm)	$S$ (fm)	$R$ (km)
0.01	0.00000	92.582884	-7.77718	5.45906	0.23478	12.6120
	-0.50000	79.602084	-7.83860	5.45937	0.23687	13.1190
0.02	0.00000	95.023504	-7.78256	5.45913	0.22827	12.2350
	-0.50000	81.396484	-7.84313	5.45928	0.23145	12.7610
0.03	0.00000	97.614400	-7.78766	5.45931	0.22182	11.9530
	-0.50000	83.283876	-7.84748	5.45928	0.22607	12.4490
0.04	0.00000	100.360324	-7.79255	5.45960	0.21542	11.7530
	-0.40000	88.021924	-7.84028	5.45937	0.21984	12.1030
0.05	0.00000	103.22560	-7.79745	5.46002	0.20901	11.6100
	-0.40000	90.212004	-7.84461	5.45960	0.21430	11.9140
0.06	0.00000	106.29610	-7.80200	5.46053	0.20267	11.5040
	-0.40000	92.544400	-7.84865	5.45990	0.20881	11.7690
0.08	0.00000	112.954384	-7.81084	5.46188	0.19004	11.3630
	-0.30000	101.123136	-7.84530	5.46099	0.19613	11.5130
0.10	0.00000	120.56040	-7.81876	5.46361	0.17751	11.2750
	-0.20000	111.386916	-7.84152	5.46268	0.18260	11.3530

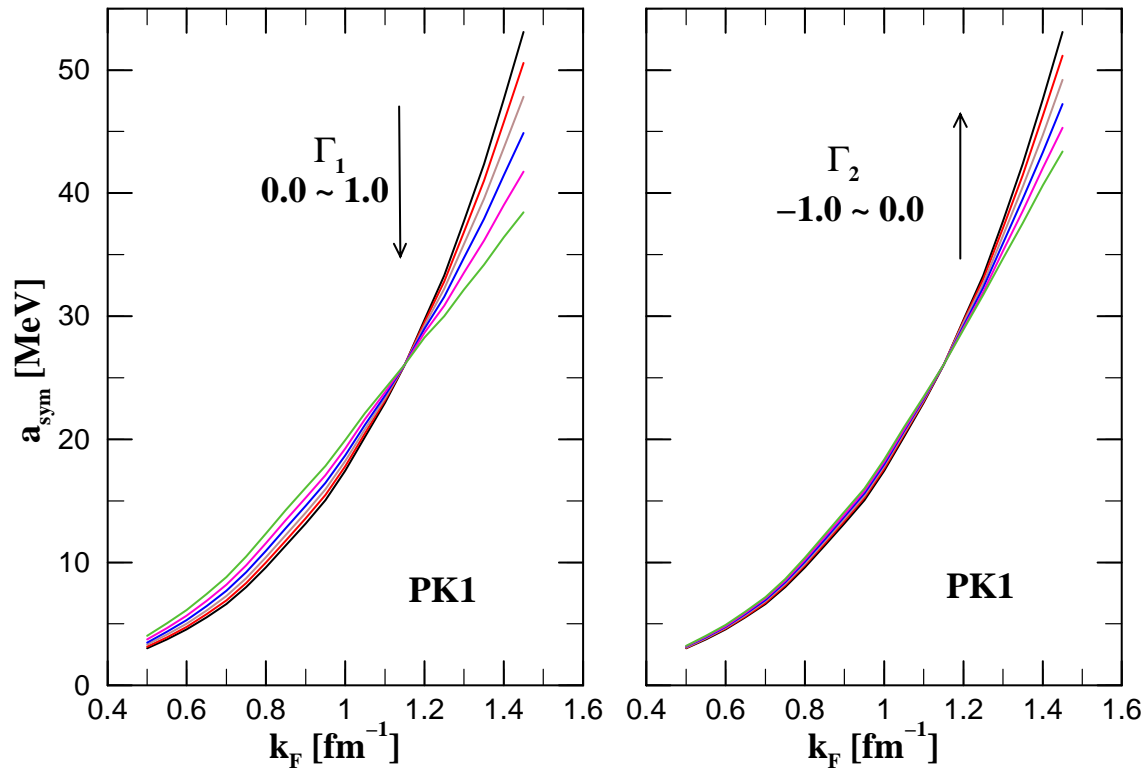


FIG. 1: (Color online) The symmetry energy,  $a_{sym}$  (in MeV), in symmetric nuclear matter as a function of the Fermi momentum,  $k_F$  (in  $\text{fm}^{-1}$ ), after adding different values of  $\Gamma_1$  (left panel) or  $\Gamma_2$  (right panel) terms to the original PK1 effective interaction. The direction of the arrows indicates values of increasing  $\Gamma_1$  and  $\Gamma_2$ .

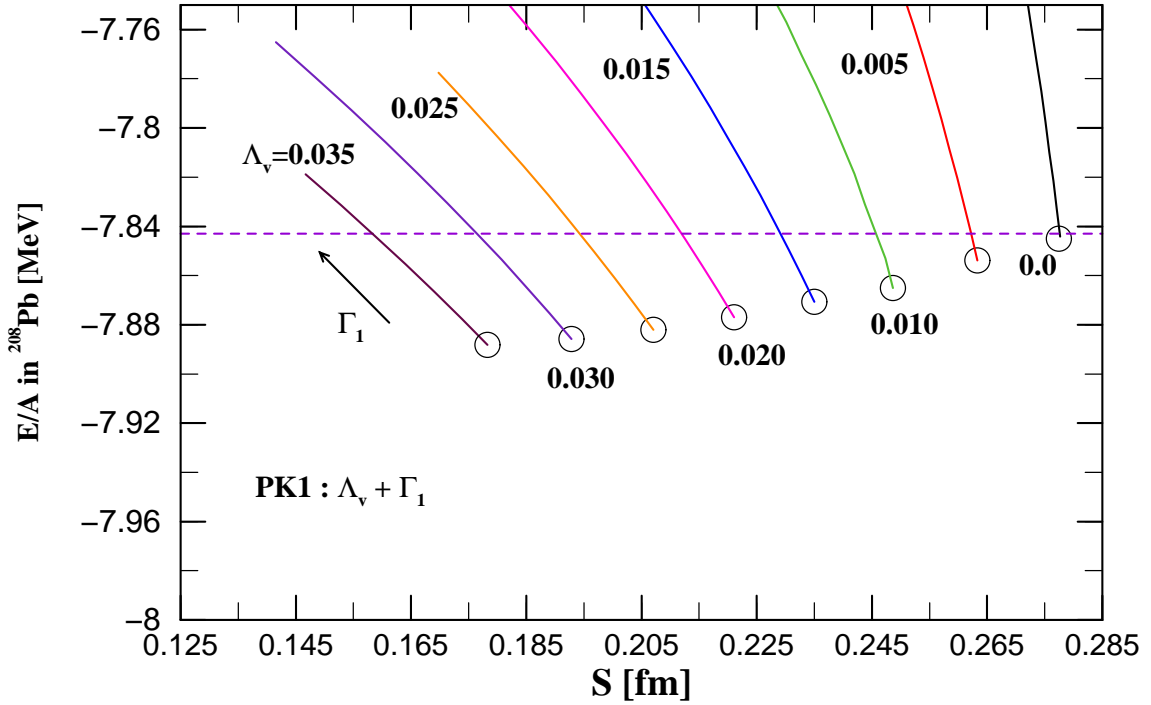


FIG. 2: (Color online) Binding energy per nucleon,  $E/A$  (in MeV), versus neutron skin thickness,  $S$  (in fm), in  $^{208}\text{Pb}$  for the PK1 effective interaction for different combinations of  $\Lambda_v$  and  $\Gamma_1$ , with  $\Gamma_2 = 0$ . The direction of the arrow next to the various lines corresponds to increasing values of  $\Gamma_1$ . The open circles denote the results for  $\Gamma_1 = 0$ . The horizontal dashed line corresponds to the experimental binding energy per nucleon.

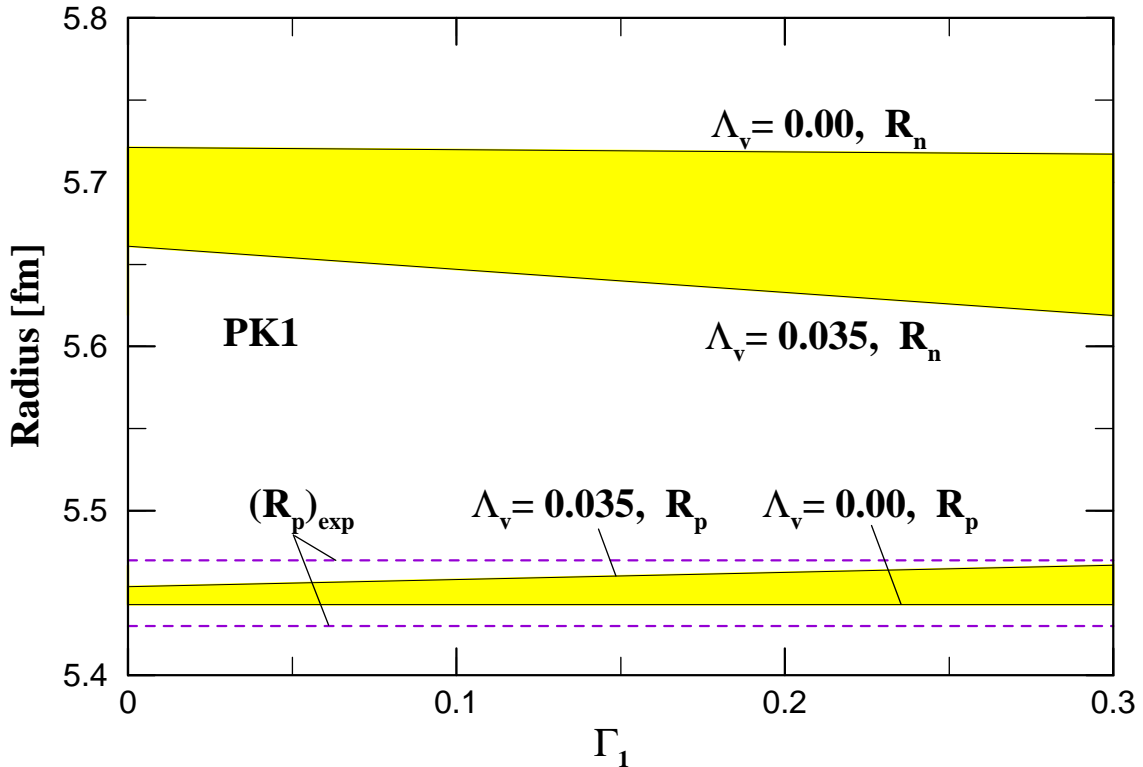


FIG. 3: (Color online) Proton and neutron radii,  $R_p$  and  $R_n$  respectively, in  $^{208}\text{Pb}$  for the PK1 effective interaction for different combinations of  $\Lambda_v$  and  $\Gamma_1$ , with  $\Gamma_2 = 0$ . The shaded regions denote the variation in the values of the radii associated with different combinations of these parameter sets. Also indicated, by the dashed horizontal lines, are the lower and upper limits associated with the experimentally extracted value of the proton radius.

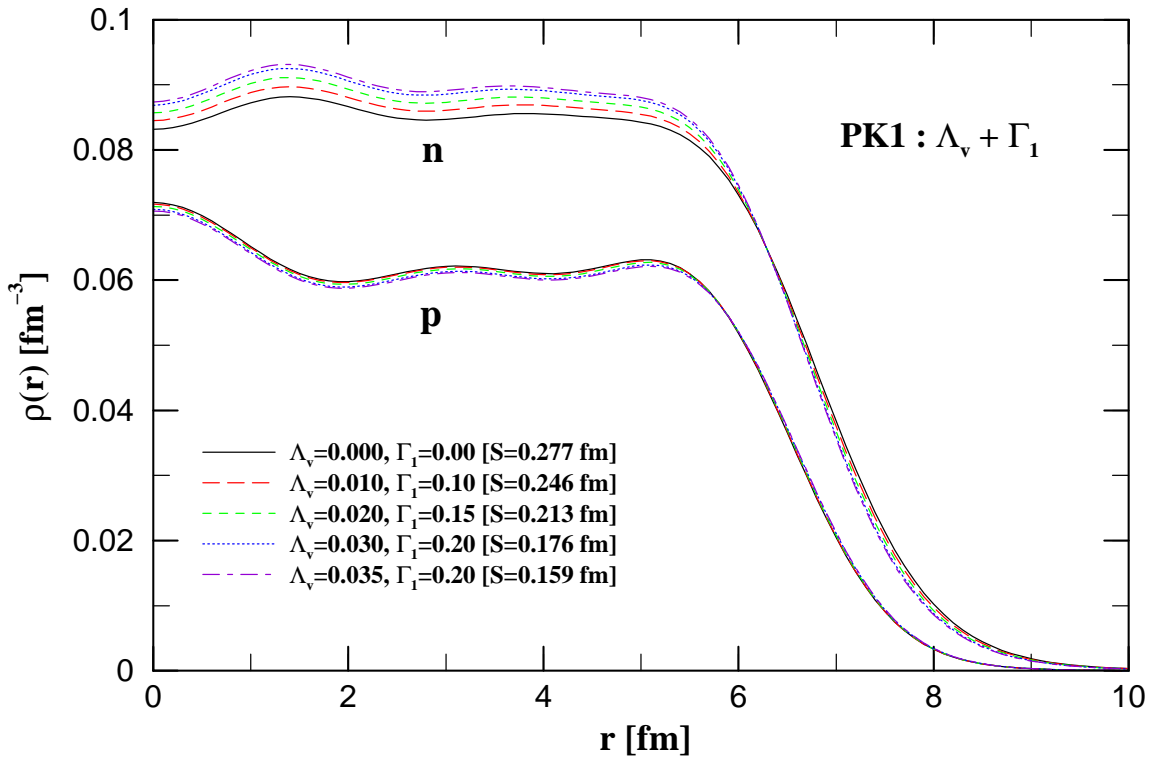


FIG. 4: (Color online) Neutron,  $n$ , and proton,  $p$ , density distributions (in  $\text{fm}^{-3}$ ) in  $^{208}\text{Pb}$  for the PK1 effective interaction for combinations of  $\Lambda_v$  and  $\Gamma_1$ , with  $\Gamma_2 = 0$ , which reproduce the experimental binding energy per nucleon for  $^{208}\text{Pb}$ . The value in square brackets indicates the neutron skin thickness,  $S$ , corresponding to a specific parameter set.

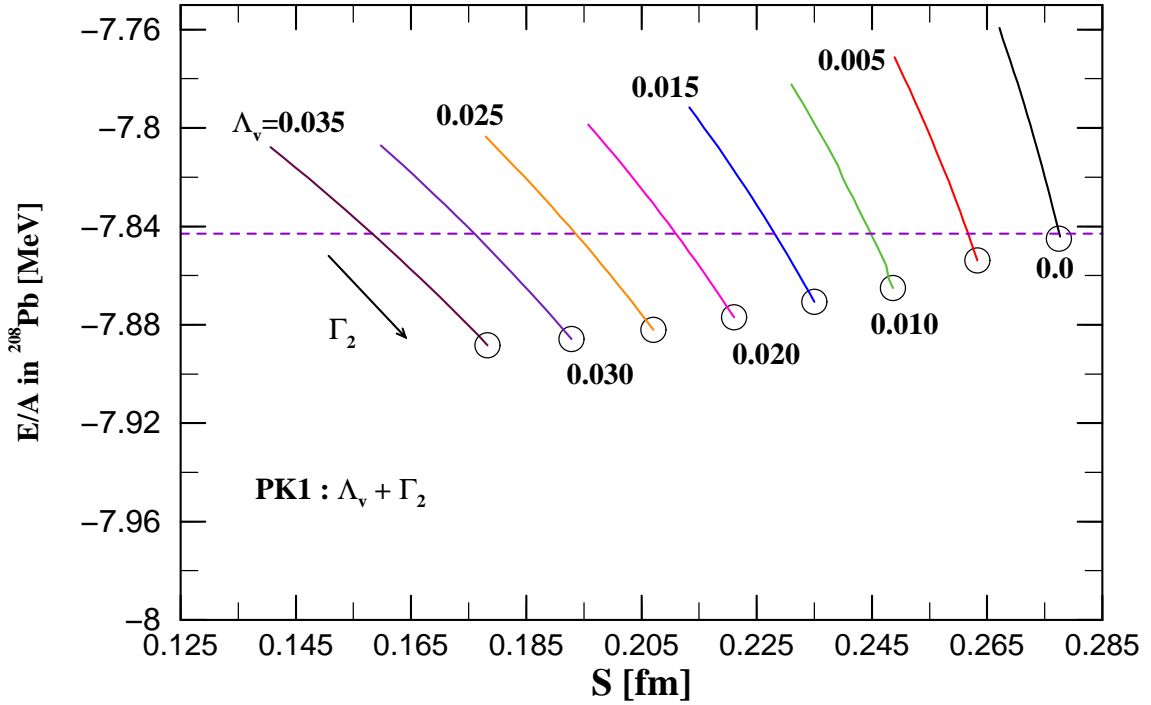


FIG. 5: (Color online) Binding energy per nucleon,  $E/A$  (in MeV), versus the neutron skin thickness,  $S$  (in fm), in  $^{208}\text{Pb}$  for the PK1 effective interaction for different combinations of  $\Lambda_v$  and  $\Gamma_2$ , with  $\Gamma_1 = 0$ . The direction of the arrow next to the various lines corresponds to increasing values of  $\Gamma_2$ . The open circles denote the results for  $\Gamma_2 = 0$ . The horizontal dashed line corresponds to the experimental binding energy per nucleon.

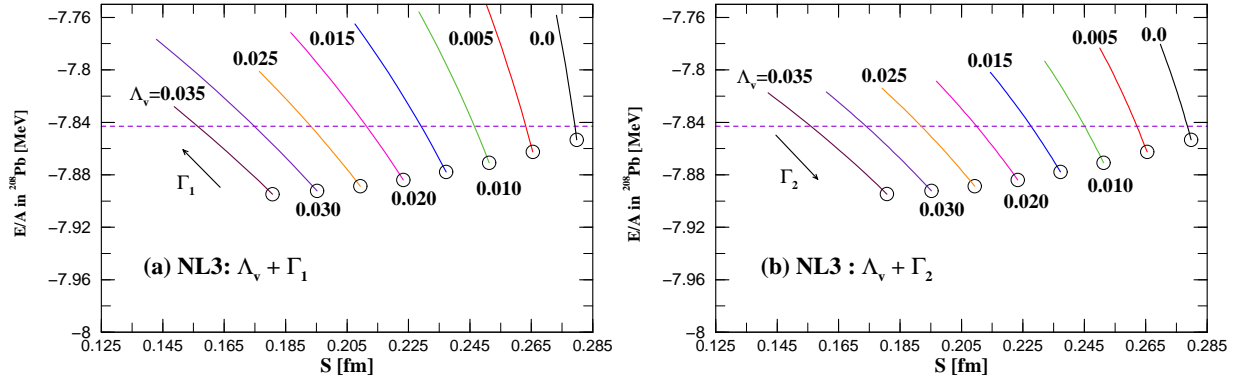


FIG. 6: (Color online) Binding energy per nucleon,  $E/A$  (in MeV), versus neutron skin thickness,  $S$  (in fm), in  $^{208}\text{Pb}$  for the NL3 effective interaction for different combinations of (a)  $\Lambda_v$  and  $\Gamma_1$  (left panel), with  $\Lambda_2 = 0$ , and (b)  $\Lambda_v$  and  $\Gamma_2$  (right panel), with  $\Lambda_1 = 0$ . The direction of the arrows next to the various lines corresponds to increasing values of  $\Gamma_1$  ( $\Gamma_2$ ). The open circles denote the results for  $\Gamma_1 = 0$  ( $\Gamma_2 = 0$ ). The horizontal dashed line corresponds to the experimental binding energy per nucleon.

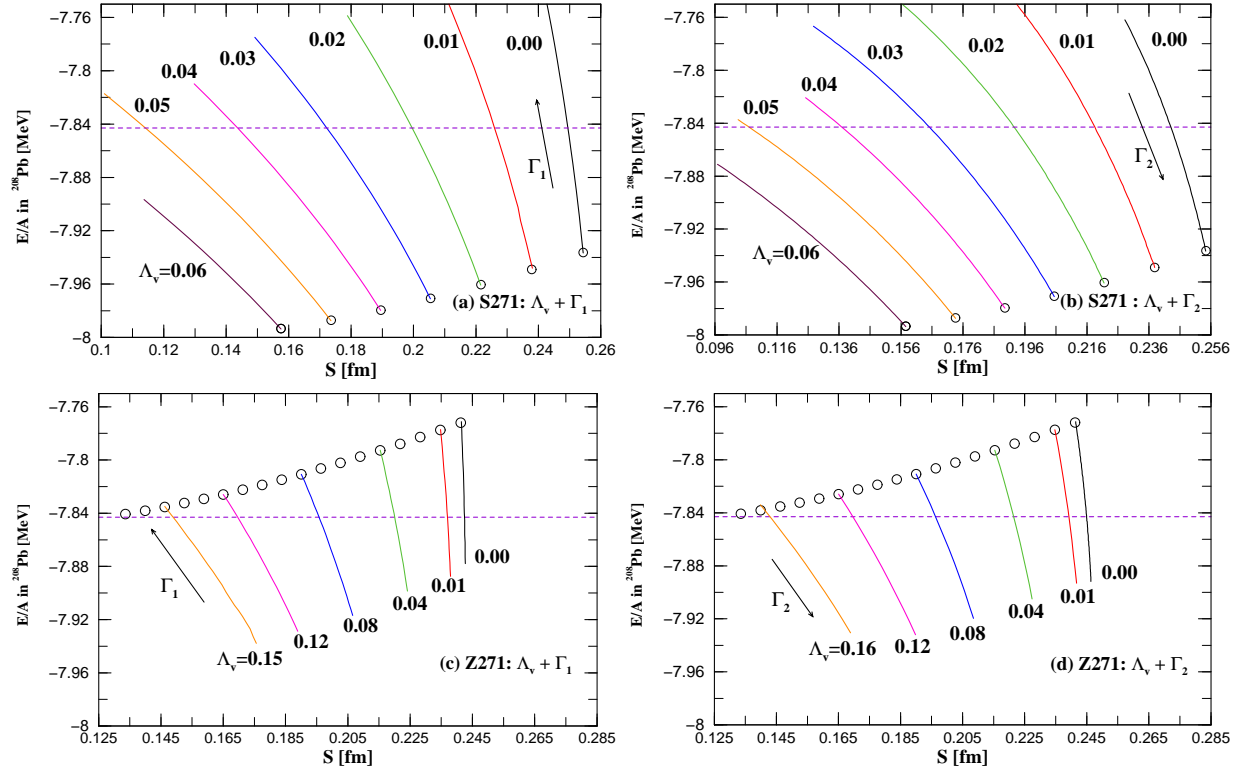


FIG. 7: (Color online) Binding energy per nucleon,  $E/A$  (in MeV), versus neutron skin thickness,  $S$  (in fm), in  $^{208}\text{Pb}$  for the (a) S271 effective interactions for different combinations of  $\Lambda_v$  and  $\Gamma_1$  (left panel), with  $\Lambda_2 = 0$ ; (b) S271,  $\Lambda_v$  and  $\Gamma_2$  (right panel), with  $\Lambda_1 = 0$ ; (c) Z271,  $\Lambda_v$  and  $\Gamma_1$  (left panel), with  $\Lambda_2 = 0$ ; (d) Z271,  $\Lambda_v$  and  $\Gamma_2$  (right panel), with  $\Lambda_1 = 0$ . The direction of the arrows next to the various lines corresponds to increasing values of  $\Gamma_1$  ( $\Gamma_2$ ). The open circles denote the results for  $\Gamma_1 = 0$  ( $\Gamma_2 = 0$ ). The horizontal dashed line corresponds to the experimental binding energy per nucleon.

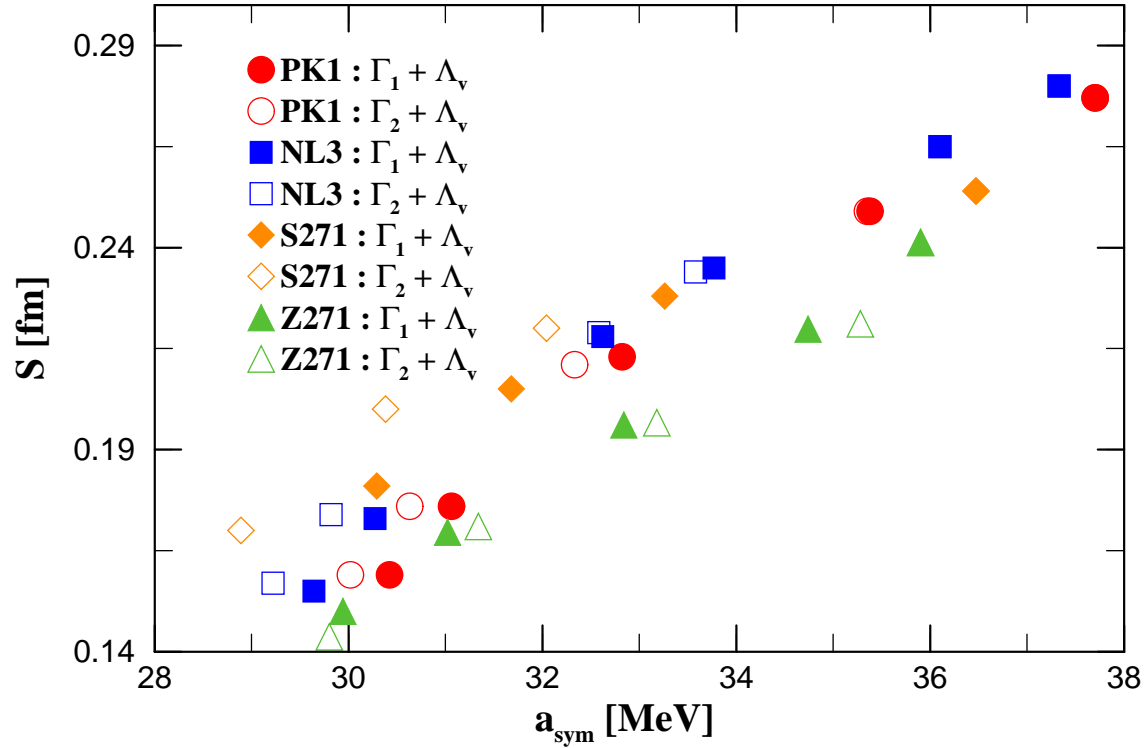


FIG. 8: (Color online) Neutron skin thickness,  $S$  (in fm), in  $^{208}\text{Pb}$  versus the symmetry energy,  $a_{sym}$  (in MeV), of nuclear matter at saturation density for the PK1, NL3, S271, and Z271 effective interactions for various combinations of  $\Lambda_v$  and  $\Gamma_1$  ( $\Gamma_2$ ), which reproduce the experimental binding energy per nucleon for  $^{208}\text{Pb}$ .

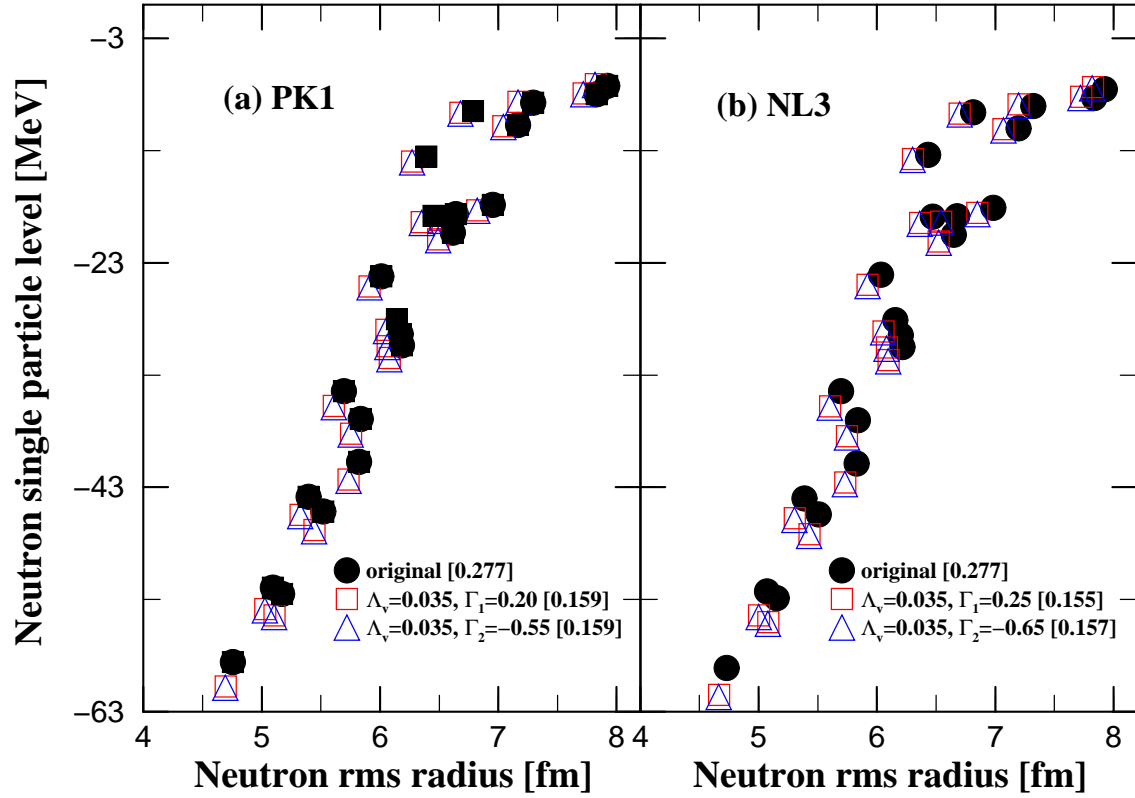


FIG. 9: (Color online) Neutron single particle energy levels (in MeV) versus their corresponding neutron rms radii (in fm) in  $^{208}\text{Pb}$  for the (a) PK1 and (b) NL3 effective interactions: original one ( $\Lambda_v = \Gamma_1 = \Gamma_2 = 0$ ) denoted by filled circles, as well as for specific combinations of  $\Lambda_v$  and  $\Gamma_1$  (open squares), with  $\Gamma_2 = 0$ , and also  $\Lambda_v$  and  $\Gamma_2$  (open triangles), with  $\Gamma_1 = 0$  which yield a minimum value for  $S$  (in square brackets) for the corresponding combinations of parameters.

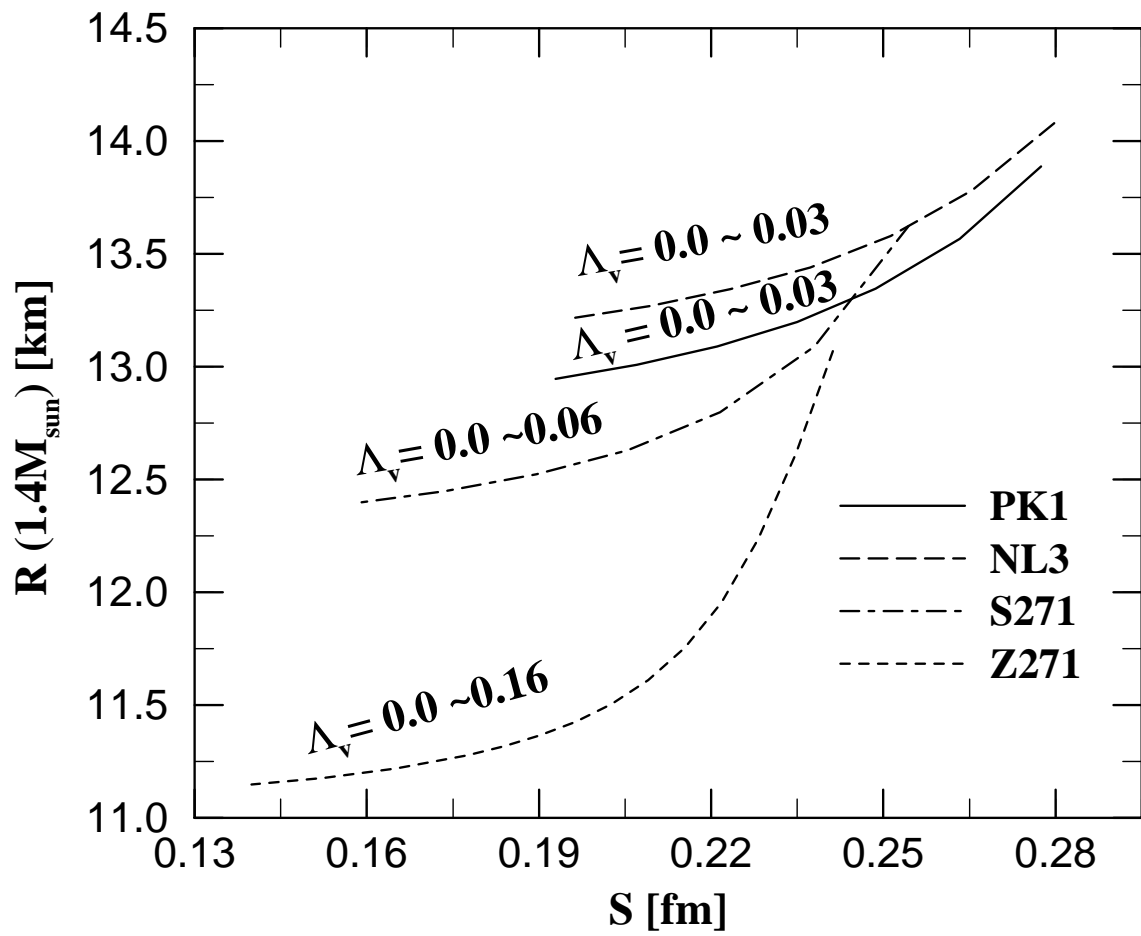


FIG. 10: The radius,  $R$  (in km), of a 1.4 solar-mass neutron star versus the neutron skin thickness,  $S$  (in fm), in  $^{208}\text{Pb}$  for the PK1, NL3, S271, and Z271 effective interactions for different ranges of values of  $\Lambda_v$ , indicated next to the various line types.

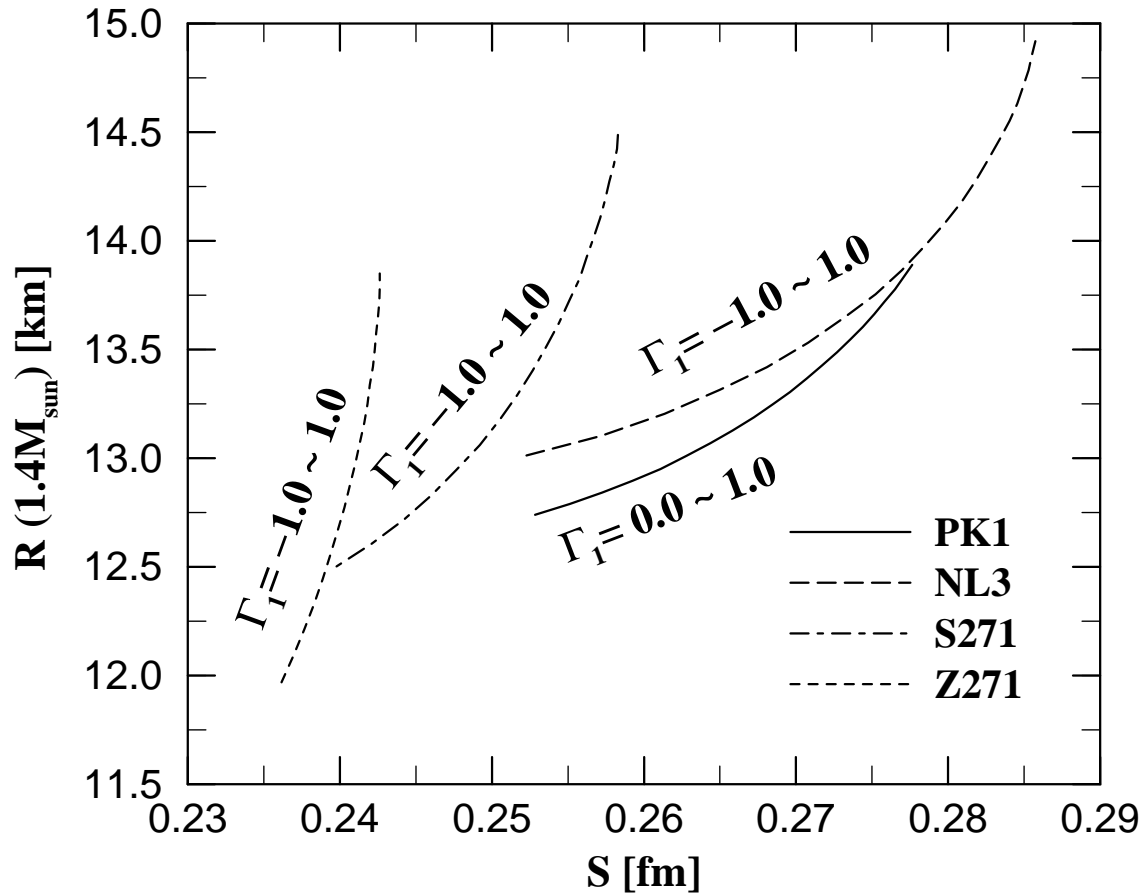


FIG. 11: The radius,  $R$  (in km), of a 1.4 solar-mass neutron star versus the neutron skin thickness,  $S$  (in fm), in  $^{208}\text{Pb}$  for the PK1, NL3, S271, and Z271 effective interactions for different ranges of values of  $\Gamma_1$ , indicated next to the various line types.

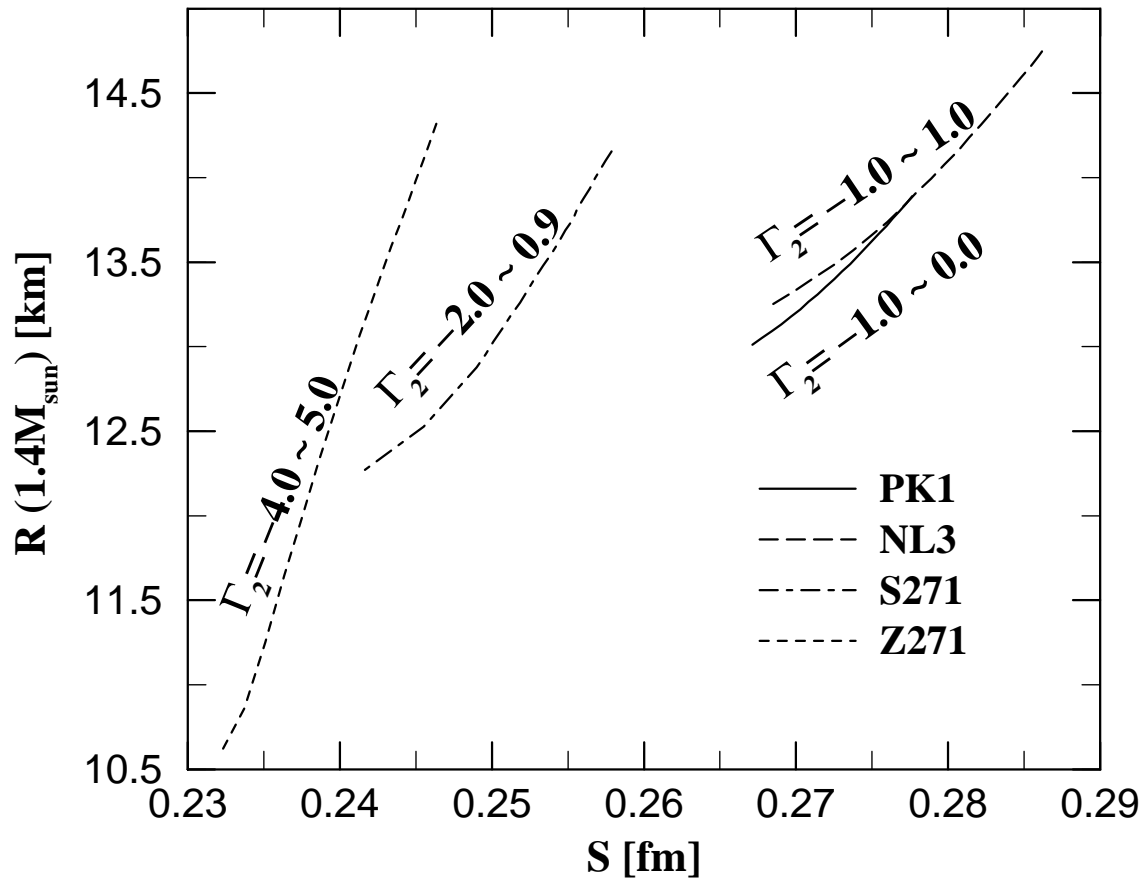


FIG. 12: The radius,  $R$  (in km), of a 1.4 solar-mass neutron star versus the neutron skin thickness,  $S$  (in fm), in  $^{208}\text{Pb}$  for the PK1, NL3, S271, and Z271 effective interactions for different ranges of values of  $\Gamma_2$ , indicated next to the various line types.

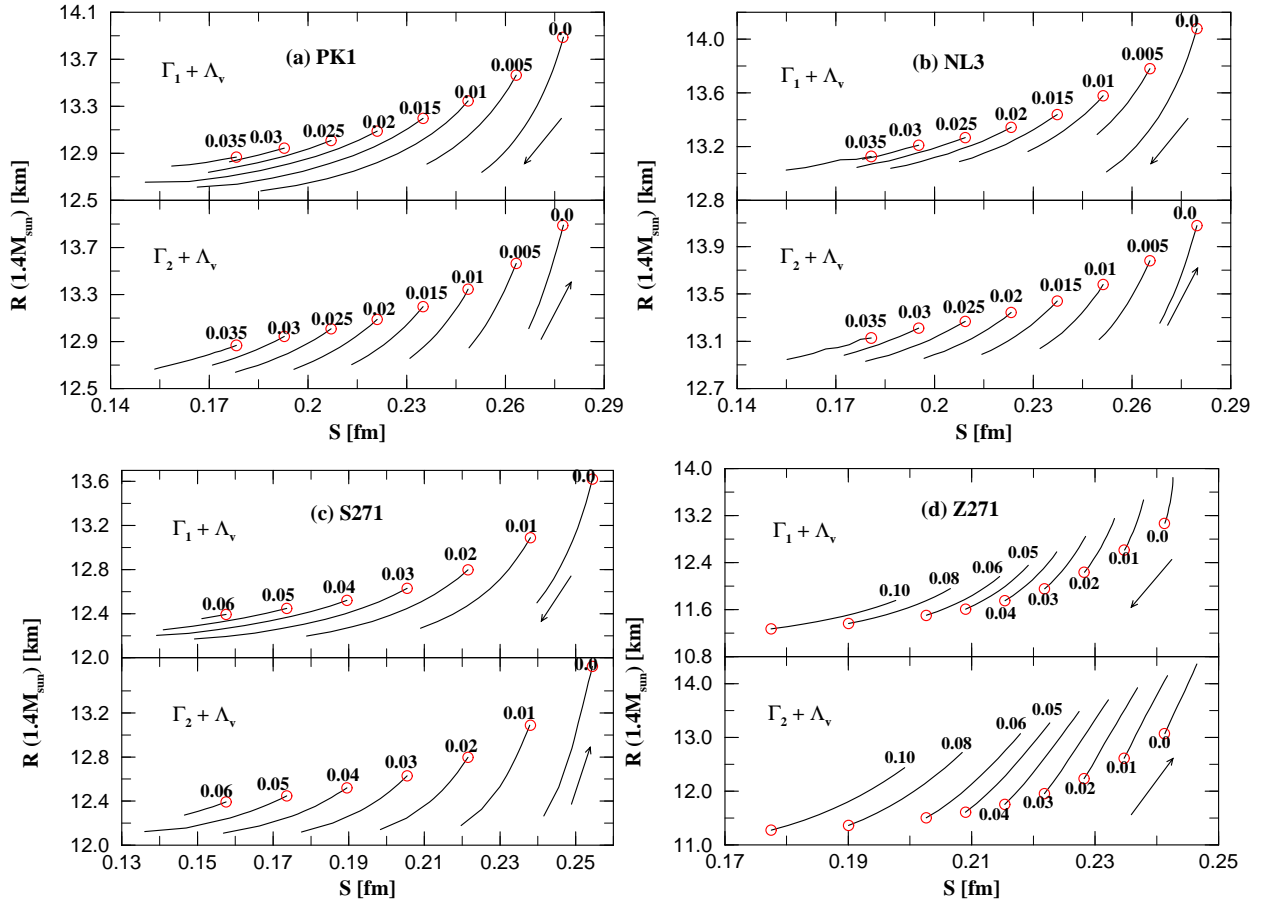


FIG. 13: (Color online) The radius,  $R$  (in km), of a 1.4 solar-mass neutron star versus the neutron skin thickness,  $S$  (in fm), in  $^{208}\text{Pb}$  for the (a) PK1, (b) NL3, (c) S271, and (d) Z271 effective interactions for various combinations of  $\Lambda_v$ ,  $\Gamma_1$  and  $\Gamma_2$ . The upper panels are associated with the  $\Lambda_v$  and  $\Gamma_1$ , with  $\Gamma_2 = 0$ , combination: open circles denote values corresponding to  $\Gamma_1 = 0$  and the direction of the arrows indicates values of increasing  $\Gamma_1$ . The lower panels are associated with the  $\Lambda_v$  and  $\Gamma_2$ , with  $\Gamma_1 = 0$ , combination: open circles denote values corresponding to  $\Gamma_2 = 0$  and the direction of the arrows indicates values of increasing  $\Gamma_2$ .